2008

Characterization and optimization of detector components and measurement procedures for the near detector of the T2K neutrino long baseline experiment

Kevin McBryde
Louisiana State University and Agricultural and Mechanical College, mcbryde_kevin@yahoo.com

CHARACTERIZATION AND OPTIMIZATION OF DETECTOR COMPONENTS AND MEASUREMENT PROCEDURES FOR THE NEAR DETECTOR OF THE T2K NEUTRINO LONG BASELINE EXPERIMENT

A Thesis

Submitted to the Graduate Faculty of the
Louisiana State University and
Agricultural and Mechanical College
in partial fulfillment of the
requirements for the degree of
Master of Science

in

The Department of Physics & Astronomy

by
Kevin McBryde
B.A., University of Colorado, 2004
August 2008

Acknowlegements

Thank you to my advisor, Thomas Kutter; to my committee members Bill Metcalf and David Young; to others in the lab and the LSU T2K group past and present: Jason Goon, Brandon Hartfiel, Jason Anderson, Jessica Brinson, Jarek Nowak, Joey Chatelain, Guofeng Yuan, and Dale Little; to Brad Ellison and Randy Gould at the LSU Electronics Shop and George Gascon at the LSU Machine Shop. This thesis would never have been completed without all of you! Thank you! This work received financial support from the U.S. Department of Energy.

Table of Contents

List of Tables

List of Figures

Abstract

T2K (Tokai to Kamioka) is the first off-axis long baseline neutrino oscillation experiment, and its primary goal is to measure the neutrino mixing parameter θ_{13}. A beam of muon type neutrinos with mean energy 600 MeV will be directed from the proton synchrotron at JPARC toward the Super-Kamiokande detector 295 km away. A near detector will be located 280 m from the proton beam target and instrumented with sub-detectors for measuring neutrino interactions prior to oscillation. One of these sub-detectors, the side muon range detector (SMRD), will help in measuring the neutrino energy spectrum and identifying backgrounds and also will serve as a cosmic ray muon trigger for calibrations of other sub-detectors. The SMRD will consist of approximately 2000 scintillator slabs distributed inside the iron return yokes for the magnetic field which surrounds the other sub-detectors. The scintillators will be read out via Si-based solid state photosensors.

A number of relevant parameters for the photosensors have been measured and the results are presented here. The gain and dark rate have been determined as a function of threshold, bias voltage, and operating temperature. The Si-based photosensors are a new technology that has not been used on previous experiments, and their longevity has been in question especially since T2K will run for approximately ten years. So we have also heated the photosensors to 80 °C for a number of months to accelerate their aging and present the long term variation in dark rate and gain. We find no significant degradation over time.

The scintillators have also been characterized; we have performed tests using atmospheric muons and radioactive sources to develop a testing procedure to determine scintillator quality and to reject inferior modules prior to installation. The effect on total light yield of fiber alignment, fiber polishing, gluing the fiber into the scintillator, and fiber damage have been measured. We find that triggering on muons under optimal conditions, the light yield is about 40 photoelectrons. We also conclude that major damage will be detectable using gammas from a source although minor damage may be more difficult to detect.

Chapter 1

Introduction

Neutrino physics is one of the most important fields in physics today. Particle physicists study the neutrino in its own right and how it falls into the framework of the other fundamental particles, but the study of this enigmatic particle is important to many other disciplines as well. A better understanding of neutrinos and their properties has implications for fields as diverse as cosmology, astrophysics, geology, and quantum gravity. The neutrino provides astrophysicists with a window into the inner-workings of supernovae and the core of our own sun. The physical properties and composition of the Earth's own core may be studied by geologists using neutrinos. Cosmologists cite the neutrino as the only means to observe the high-energy universe above the point where cosmic rays interact with the cosmic microwave background. And since the neutrino only interacts via the weak and gravitational force, it may prove useful in the study of quantum gravity as well. A better understanding of the neutrino will help advance these many diverse fields, however the existence of this particle was not even confirmed until about fifty years ago.

1.1 Discovery of the Neutrino and the Standard Model of Particle Physics

The neutrino was first proposed in 1930 by Wolfgang Pauli as a theoretical solution to the missing energy problem in beta decay. Lise Meitner and Otto Hahn had observed near the beginning of the twentieth century that when neutrons decayed into protons and electrons, the resultant electrons were not monoenergetic but exhibited a continuous spectrum. This was mysterious and it appeared that the law of conservation of energy had been violated. But Pauli proposed something that might have been considered even more unusual—a massless, neutral, and (almost) unobservable particle which carries away the extra energy, later named the neutrino. The neutrino, being a chargeless lepton, does not interact by the strong or electromagnetic forces, but does interact via the weak force so it is in principle observable. But the typical cross-sections are extremely small so a very high

flux is necessary to achieve even a single detection. In fact, for neutrinos from the sun the flux is only attenuated by half through 1 light-year of lead! Because of these difficulties, the first neutrino was not observed until 1956.

There are four primary sources of neutrinos which produce sufficiently high fluxes that they can be observed in sufficient quantities to study. There are neutrinos generated in cosmic-ray showers which are called "atmospheric neutrinos"; there are neutrinos produced in nuclear reactions in the core of the sun known as "solar neutrinos"; and there are man-made sources of neutrinos produced by particle accelerators and nuclear power plants. The first neutrino experiment observed anti-neutrinos from a nearby nuclear power plant. Subsequent experiments have taken advantage of all four of these primary sources.

The neutrino associated with beta-decay is aptly named the "electron-type" neutrino. Later in the twentieth century, two other 'flavors' of neutrino were discovered. They are associated with the heavy leptons, the muon and the tau particle, and so they are called the "muon-type" and "tau-type" neutrinos. These three flavors of neutrinos (symbolically ν_e, ν_μ, ν_τ) complete the Standard Model of particle physics. This highly successful theory says that all matter in the universe is composed of some combination of six quarks and six leptons. The Standard Model is simple and beautiful but it soon became evident that its explanation of the universe is not complete.

1.2 Neutrino Oscillation

One assumption underlying the minimal Standard Model was that neutrinos have no mass. Their speed was shown to be (within experimental uncertainties) consistent with the speed of light, and in accord with the theory of special relativity, this necessarily implies zero mass. However the solution to the solar neutrino problem eventually showed this assumption to be false.

One of the earliest neutrino experiments was built to observe electron-type neutrinos from the sun. The experiment in the Homestake Mine in South Dakota was built deep underground to minimize background coming from cosmic ray showers in the atmosphere. The experiment was successful in detecting solar neutrinos, however the observed flux was only about one third of the expected flux based on solar models. This result was confirmed by other experiments. The solar models were very accurate and well understood so some physicists suspected that they lacked understanding of the neutrinos themselves.

The proposed solution drew an analogy to the already existent theory of quark mixing. The idea is that a given flavor of neutrino is actually composed of a superposition of three mass eigenstates. So instead of ν_e, ν_μ, ν_τ, there exists some mixture of the mass eigenstates ν_1, ν_2, ν_3 which only collapses to one of the flavor-states when interacting with matter. The neutrinos then oscillate during propagation among the three flavor-states. A ν_e produced in the sun could therefore oscillate to a ν_μ or a ν_τ in route to the earth. If the mixing were maximal then this would explain why only one third of the expected flux was observed in

a detector only designed for electron-type neutrinos. This theory, then, is an extension of the Standard Model because, if neutrinos are composed of the three mass-eigenstates, they cannot be massless. In order to test the new model, a new detector had to be built which was sensitive to all three types of neutrinos. If the observed flux was that predicted by the solar neutrino models, then the theory of Neutrino Oscillation would be confirmed. The Sudbury Neutrino Observatory (SNO)[7] was the experiment which fulfilled this role.

Other experiments observed oscillations in atmospheric neutrinos (Super-Kamiokande)[8], in reactor neutrinos (KamLAND)[9] and in neutrinos produced in a particle accelerator (LSND [6], K2K [9], MINOS [5], MiniBooNE [2]). The next job of physicists is to accurately measure the oscillation parameters.

1.3 Measuring the Oscillation Parameters

One of the two possible mass hierarchies is shown schematically in Figure 1.1. [1] The diagram depicts each of the mass eigenstates as a horizontal bar with varying composition of flavor states represented as dashed regions. Two of the eigenstates are relatively close in mass while the separation between these and the third mass is much larger. It should be noted that the sign of these mass differences has not been determined so the hierarchy depicted may be inverted. It is the squares of the mass differences that can be measured in neutrino oscillation physics experiments. We can calculate the probability that a neutrino of one type will oscillate as it propagates. The approximate probability of oscillation of ν_μ to ν_e (ignoring Δm^2_{21}, CP violation, and matter effects) is given in equation 1.1. [1] It is usually sufficient to use this approximation because the neglected effects are small.

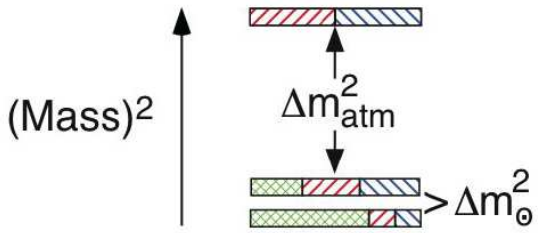

Figure 1.1: Mass hierarchy for three-neutrino mixing. Green cross-hash represents ν_e, red left-leaning hash represents ν_μ, and green right-leaning hash represents ν_τ.

$$P(\nu_\mu -> \nu_e) = sin^2(2\theta_{13})sin^2(\theta_{23})sin^2(\Delta m^2_{32}L/4E) \tag{1.1}$$

The most recent values for the neutrino oscillation parameters based on a global analysis

Table 1.1: Values of the neutrino oscillation parameters

Parameter	Value with Uncertainty
Δm^2_{21}	$(8.0^{+0.4}_{-0.3}) \times 10^{-5} eV^2$
Δm^2_{23}	1.9 to 3.0 $\times 10^{-3} eV^2$ (90% CL)
$sin^2(2\theta_{12})$	$0.86^{+0.03}_{-0.04}$
$sin^2(2\theta_{23})$	> 0.92 (90% CL)
$sin^2(2\theta_{13})$	< 0.19 (90% CL)

of results from many experiments are shown in Table 1.1. [1] The table shows that only an upper bound is known for the third mixing angle θ_{13}. The primary goal of T2K (Tokai to Kamioka), a next generation neutrino long baseline experiment, is to determine the value of θ_{13}. This will be accomplished by studying oscillations of muon-type neutrinos produced in a particle accelerator. Equation 1.1 shows that the appearance of electron-type neutrinos given a beam of pure muon-type neutrinos depends on L/E (the distance of propagation over the energy). So it is necessary to measure not only the composition of the beam before and after oscillation, but also the energy of the beam of neutrinos, in order to determine the value of θ_{13}.

Chapter 2

Neutrino Detection at T2K

2.1 JPARC and the Beam

T2K will make use of the JPARC facility on the eastern coast of Japan which will house a 50 GeV proton synchrotron. The high-energy protons will be sent through a target ejecting pions and other particles. The charged secondary particles will be focussed by means of a magnetic field. Some of the pions decay to muons and muon-type neutrinos in the decay pipe and the remainder are absorbed at the end of the decay region. The muons will be ranged out in the ground leaving a nearly pure ν_μ beam.

2.2 The Far Detector (Super-Kamiokande)

295 km away from JPARC lies the far detector, Super-Kamiokande, the world's largest water-Cherenkov neutrino detector. It was originally built to search for proton decay, but soon became the premier facility for observing solar and atmospheric neutrinos. Super-Kamiokande was the first experiment to verify that neutrinos do in fact oscillate. It is built underground beneath 1000 m water-equivalent of rock to reduce background from cosmic-ray showers. In 2001 more than half of its original 10,000 PMTs were destroyed by a shock wave in the water. The PMTs have since been replaced and the detector is ready for its second life as the far detector for T2K.

2.3 INGRID (The On-Axis Near Detector)

There will be two near detectors at JPARC to observe the neutrino beam properties prior to oscillation. The INGRID detector is on the axis of the beam and ND280 is off-axis in

the direction of the far detector. INGRID will measure the neutrino flux and the direction of the main axis of the beam. The beam direction must be measured to within 0.5 mrad to reduce the systematic errors of neutrino flux and energy at the far detector to 2% and 3% respectively.

2.4 ND280 (The Off-Axis Near Detector)

The far detector is not located on the beam axis but rather about three degrees off-axis. This is done because the neutrino energy spectrum is narrower off-axis than on-axis and there are fewer non-ν_μ background neutrinos. The ND280 detector is located along this off-axis part of the beam. It will consist of a number of sub-detectors: the Pi-Zero, the Tracker, the ECAL, and the SMRD (see Figure 2.1).

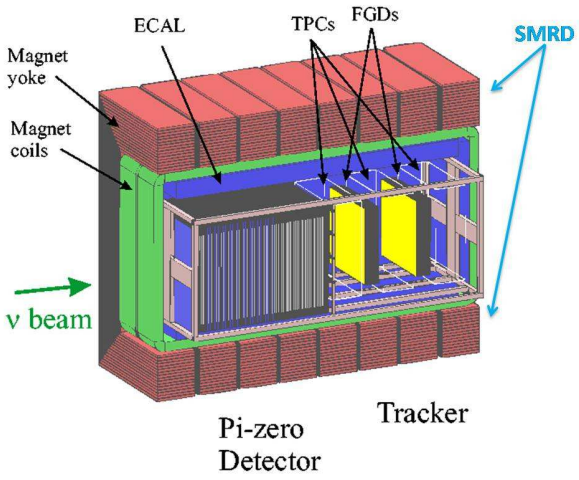

Figure 2.1: Schematic diagram of the ND280 detector complex.

2.4.1 Pi-Zero, Tracker, ECAL

There will be four subdetectors at the ND280 off-axis site. The first of these is called the POD (π^0 Detector). This subdetector will measure background associated with pions produced by neutrino interactions in water. Since π^0s decay into photons they could be mistaken for electron-neutrino events in the far detector so this background must be considered. The POD will consist of scintillating bars and water modules layered in a "pancake" fashion, alternating water layer with scintillating layer.

The Tracker consists of three TPCs (Time Projection Chambers) for tracking charged particles and two FGDs (Fine-Grained Detectors) wherein the charged particles are produced by charged-current interactions. The primary goals of the Tracker are to measure the neutrino energy spectrum and reconstruct the path of charged pions and protons. The FGD

is similar to the POD in that it consists of water layers alternating with layers of organic scintillator.

The ECAL (Electromagnetic Calorimeter) is for the detection of photons produced in π^0 decays. This subdetector, which consists of sandwiched lead and scintillator, will surround the POD and Tracker. The three inner subdetectors will be enclosed in magnet coils providing a 0.2 Tesla magnetic field in the direction perpendicular to the beam direction. This will allow for an energy determination of charged particles. There will be eight iron return yokes on each side of the detector.

2.4.2 SMRD

The SMRD (Side Muon Range Detector) has the three goals of contributing to the measurement of the neutrino energy spectrum, identifying backgrounds, and triggering on cosmic-ray muons for calibrations. These goals will be accomplished by observing muons using scintillation detectors. Each scintillator module will consist of an organic scintillator slab (in which through-going charged particles produce light), a wavelength-shifting fiber to guide the light out of the scintillator, and a photosensor to detect the light at each end of the fiber. The modules will be inserted into slots in iron yokes surrounding the other ND280 sub-detectors (see Figure 2.2).

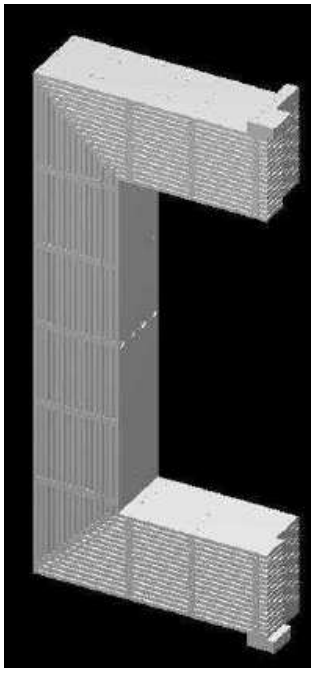

Figure 2.2: Diagram of one of the SMRD iron yokes.

The energy of forward muons will be measured by the TPC, but muons travelling at an angle to the beam will be measured by the SMRD instead. The depth of penetration into

the iron yokes will give an estimate of the energy. Since SMRD will instrument several layers in the yokes with scintillators, this will be a measurable quantity. Accomplishing this goal requires the SMRD to have a high detection efficiency and instrument enough slots with scintillators to range out the muons (approximately 2000 scintillators in total are required to meet this goal).

The muons interact in the scintillator via the charged current quasi-elastic (CCQE) interaction: $\nu_\mu + n \rightarrow \mu^- + p$. So in measuring the muon energy for these events, we can extrapolate back to the corresponding neutrino energy. Ignoring the Fermi momentum of the target n, the neutrino energy is related to the muon energy by Equation 2.1 [2]:

$$E_\nu = \frac{2(M_n - E_B)E_\mu - (E_B^2 - 2M_nE_B + m_\mu^2 + \Delta M^2)}{2((M_n - E_B) - E_\mu + p_\mu cos\theta_\mu)} \tag{2.1}$$

where m_μ, M_n, and M_p are the muon, neutron, and proton mass, respectively. E_μ, p_μ, and θ_μ are the reconstructed muon energy, momentum, and scattering angle, respectively, $\Delta M^2 = M_n^2 - M_p^2$ and E_B is the nucleon binding energy which is greater than zero.

ND280 is near the surface of the ground so, unlike at the far detector, there will be a significant flux of atmospheric muons from cosmic ray air showers. These muons may be detected by the ND280 subdetectors and a small fraction may be mistaken for muons from the beam interactions so it is important to veto these events. The flux of these muons peaks at the zenith position and falls off as cosine squared of the zenith angle so almost all of the muons will be following a vertical (or near vertical) trajectory. The SMRD will look for a coincidence between scintillators at the top of the yokes with those at the bottom of the yokes to detect these atmospheric muons.

In this work we have tested the photosensors and scintillators to be used in the SMRD. Chapter 3 presents measurement results for the photosensors. Since the POD, ECAL and FGD will also use the same photosensors as the SMRD, these measurements will also be of interest to those involved with these other subdetectors. Chapter 4 will present measurement results for the scintillators used in the SMRD.

Chapter 3

SMRD Photodetectors

A number of requirements must be fulfilled by the photosensors of SMRD to realize the science goals of the experiment. First, the light levels expected for muons traversing the scintillators is expected to be low. While many photons are produced in each traverse, less than a few dozen photons remain after absorption in the scintillator and wavelength-shifting fiber. In order to observe the passage of a muon, the device must have a high photon detection efficiency. Ordinarily, as in other similar experiments, Photo-Multiplier Tubes (PMTs) would be used for such an application. However in the SMRD this is not the ideal device for a number of reasons. One reason they are not ideal is due to the high magnetic field present in the SMRD. The magnetic field in the yokes will be about 0.2 Tesla. PMTs amplify a single photoelectron to a detectable current by using a high-voltage to accelerate it through a dynode structure producing a cascade of electrons. PMTs do not operate well in high magnetic field because of the long path length the photoelectrons take through the dynode structure. The force on the moving electrons is in a direction perpendicular to their motion, so many electrons are lost and the detection efficiency is reduced. The photons could be 'piped' outside the yokes to a low magnetic field region using a fiber as has been done in some other experiments, but due to the geometry of the SMRD, the fibers would be exposed and more susceptible to accidental damage. PMTs have the further limitations that they are usually fairly large devices (several cm in size) and there is very limited space inside the detector cavity, they require a high voltage (of order 1000 V) to operate, exhibit a poor charge resolution, and are typically very expensive.

To overcome these difficulties the SMRD group has instead decided to use a new type of silicon-based photosensor. In these devices, the electron avalanche occurs in a single semiconductor layer making them immune to the effects of a magnetic field. Additionally, they are more compact than most PMTs (mm in size), they operate at a much lower voltage (50-70 V), requiring less power to operate. The charge resolution is high enough for Si-based detectors to enable counting of individual photons, and they can be produced in large quantities at a lower price than PMTs.

3.1 Physical Properties

Two candidate Si-photosensors considered for use in the SMRD were the Multi-Pixel Photon Counters (MPPCs) manufactured by Hamamatsu Photonics and the Metal-Resistance-Semiconductor Avalanche Photo-Diodes (MRS APDs) produced by Center of Perspective Technologies and Apparatus (CPTA). Both are avalanche photodiodes operated in Geiger mode, above the breakdown voltage. For testing at our lab we received ten of the Hamamatsu devices (labeled H60 through H69) and eight of the CPTA devices (the first two were labeled 0509 and 1710, with a later batch being numbered 1 through 6). Figures 3.1 and 3.2 compare the Hamamatsu MPPC number H67 to the MRS APD number 0509 life-sized and enlarged 200X through a microscope. Each device measures 1.0 mm across and each pixel is 50 μm in size. The 400 pixels of the MPPC are arranged in a square grid pattern, while the 556 pixels of the APD are arranged octagonally. The MPPCs employ a ceramic packaging while the APDs are housed in metal.

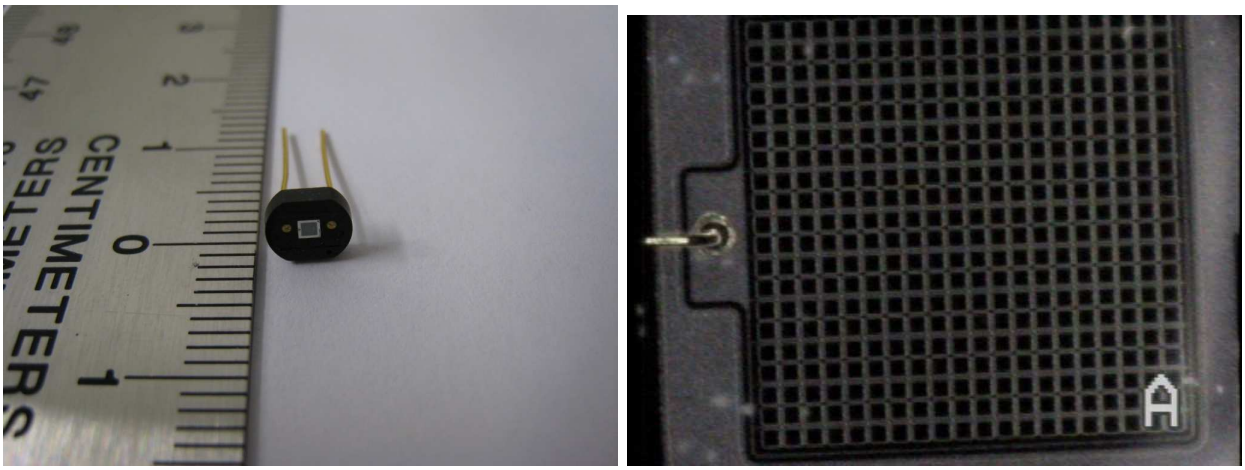

(a) (b)

Figure 3.1: Hamamatsu sensor number 67 life-size (a) and through a microscope at 200X magnification (b).

3.2 Signal Properties

A single photon incident on the sensor can produce a single photoelectron with a high quantum efficiency. This single photoelectron triggers an avalanche which results in many more electrons, a detectable current. The total number of electrons resulting from one photoelectron (1 p.e.) is referred to as the gain of the device. For the Si-based photosensor, the signals from multiple independent pixels are summed together for detection of multiple photons. So a signal from two photons (2 p.e.) should be twice as large as from one, and

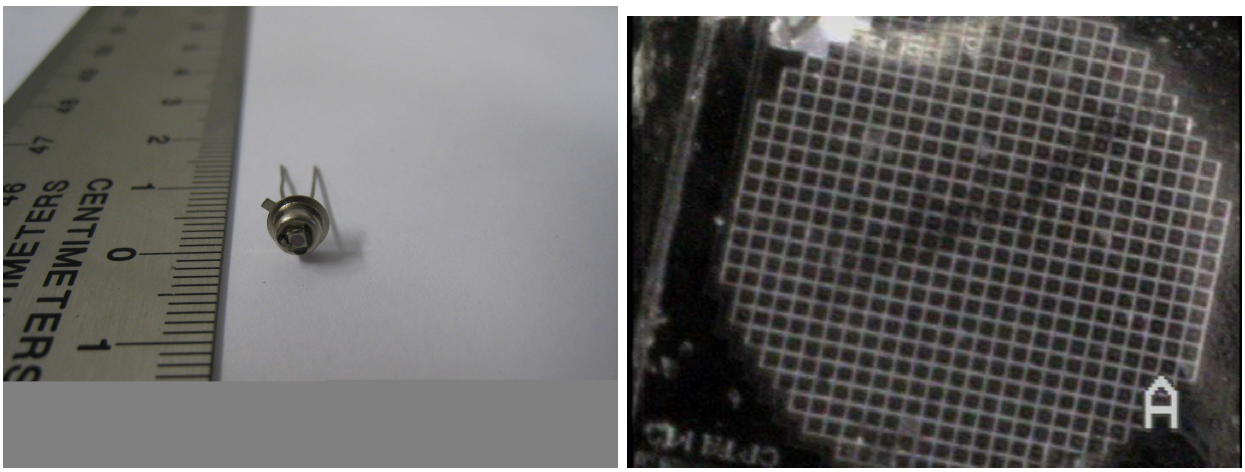

(a) (b)

Figure 3.2: MRS sensor number 0509 life-size (a) and through a microscope at 200X magnification (b).

so on. The charge spectra are not delta functions though; rather, they exhibit a Poissonian distribution about each p.e. value. Gain is dependent on temperature and bias voltage.

Electron avalanches can be triggered when a photon excites an electron into the conduction band, but avalanches can also occur in the photosensors even in a photon-free environment due to thermal excitation of electrons into the conduction band. The rate of these events not initiated by photons is called the dark rate. Dark rate is dependent on threshold which is usually set at integer multiples of 0.5 p.e. to count events above that threshold. Dark rate also depends on temperature and bias voltage. Another potential cause of avalanches is cross-talk between the pixels. This can occur when either an electron leaks through the barrier between pixels or when a photon produced in one pixel strikes an adjacent pixel. An ideal device would have a very high gain and quantum efficiency, with a very low dark rate and no cross-talk.

We now compare and contrast the the two different test sensors. We place the test sensors into a dark box which keeps out external photons from the lab. We can then use a pulsed LED to direct photons at the sensor and control the photon flux by adjusting the supply voltage for the LED. We then observe the sensor output signal using an oscilloscope. Figure 3.3 (a) shows the voltage vs. time pulse shape as seen on the oscilloscope for the Hamamatsu sensor. This can be compared with the pulse shape for the MRS device in Figure 3.3 (b). The three curves are for a threshold of 0.5, 1.5, and 2.5 p.e. respectively and are averaged over 100 traces. For a single photoelectron the typical pulse from the MRS sensors is 10 ns in duration and less than one millivolt in amplitude. For the Hamamatsu sensors the typical width is 20 ns and a similar amplitude. This small of a signal is still below the minimum threshold for our electronics (specifically the ADC), therefore the signal must be

amplified to get above this minimum threshold. We use a fast preamplifier to amplify the signal by a factor of 30 which corresponds to 20-30 mV for the first p.e. peak. The pulse shape for the Hamamatsu sensor after the preamp is shown in Figure 3.3 (c). The voltage is amplified, but the rise-time is not significantly altered.

Besides the different pulse width and physical design, there are some other key differences between the two sensors. First, due to their broader pulse width, the gain of the MPPCs is higher than for the APDs. This is an advantage because of the limited charge resolution of the electronics systems. Second, the photon detection efficiency for the MPPCs is also higher at about 50 percent, an advantage because lower energy events will be detectable. And a third advantage of the MPPCs is that the dark rate is lower; about 250 kHz at 0.5 p.e. threshold compared with about 1MHz at the same threshold for the APDs. Additionally, the reliability of the MRS APDs is in question due to the unexplained failure of five of the original eight sample devices within a few months of testing. The only real disadvantages of the MPPCs compared with the MRS APDs are their broader pulse shape (which results in poorer time resolution) and their somewhat higher bias voltage. The dark rate, gain, and reliability are more important considerations for the SMRD and so the Hamamatsu MPPCs have been chosen over the MRS APDs for use in the SMRD. Therefore, the results presented in the remainder of this chapter are for the Hamamatsu devices.

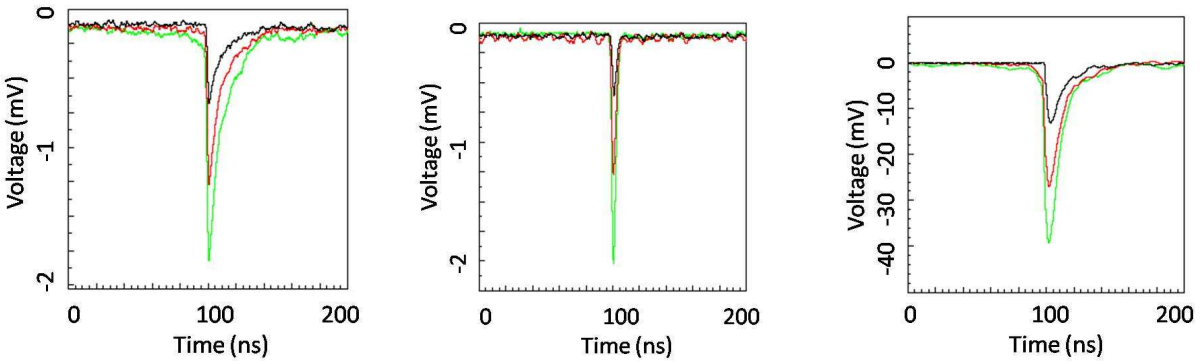

(a) Hamamatsu sensor H65 pulse shape.

(b) MRS sensor 0509 pulse shape.

(c) Hamamatsu sensor H65 pulse shape after preamplification.

Figure 3.3: Pulse shape comparison for Hamamatsu and MRS photosensors, before and after preamplification. The y-axis is in volts and the x-axis is time in ns.

3.3 LED ADC Spectra

Ultimately we will want to determine the amount of light from each scintillator in order to measure the energy and directionality of the muons. In order to count the photons, we must first know the gain of each sensor. It has been mentioned that the gain will vary with external parameters such as temperature or bias voltage so it must be measured as a function of these parameters. Integrating the voltage pulses from the sensors gives the total charge output by the sensor for each event and we can calculate the gain in number of electrons per photoelectron. This can be done in one of two ways: the first method is to save an oscilloscope trace for each event and integrate afterward in software and the second method is to use an Analog to Digital Converter (ADC) to integrate the signal electronically in real time. The advantage of saving oscilloscope traces is that we retain all timing and pulse shape information. The disadvantages are that it takes a large amount of disk space when integrating thousands of traces at high resolution and it is slow to acquire and process the data. The ADC is much faster (minutes instead of hours) and produces very small files (100s of kB instead of 100s of MB) so this is the preferable method for measuring the gain. Our ADC spectra were taken using the LeCroy 2249A Camac ADC module and read out from the crate controller using KMAX software. The LeCroy 2249A is a 10-bit resolution (1024 Channel) ADC with 0.25 pC/Channel sensitivity. The pedestal (zero-charge channel) is adjustable and is usually kept a few bins above the first ADC bin. The input impedance is $R = 50\ \Omega$ and the amplification of the preamp is $G_{pa} = 30$. Once we have measured the position of the first photoelectron peak in ADC channels, we can use Ohm's law to calculate the corresponding charge in electrons. The gain of the photosensor is then calculated using Equation 3.4.

$$V = IR \tag{3.1}$$

$$V = \frac{Q}{t}R \tag{3.2}$$

$$Q = \frac{Vt}{R} \tag{3.3}$$

$$G = \frac{(0.25pC/Ch)(ADC_{ch} - Pedestal)}{(1.6 \times 10^{-19}C/e-)G_{pa}} \tag{3.4}$$

The ADC only integrates charge during specified intervals; it must be told when to integrate and for how long. This is set by the gate. The signal is first sent through a Fan-In-Fan-Out (FIFO) where it is split into two identical copies of the original signal. One of these signals is sent to a discriminator which is used to set the gate and the other is sent through a delay module so it arrives at the ADC at the same time as the gate. Figure 3.4 shows this process schematically.

In Figure 3.5 (a) we plot the ADC spectrum from MPPC H65 triggering on dark events. The gate is 106 ns. Figure 3.5 (b) shows the spectrum for the same sensor triggering on an

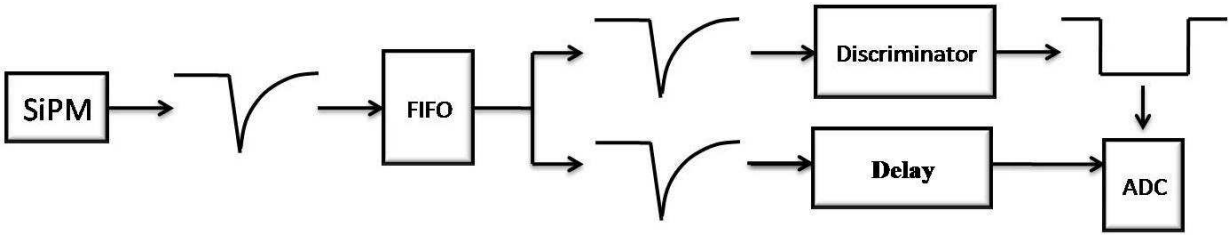

Figure 3.4: Signal path from photosensor to ADC.

LED. In this instance, a 550 nm wavelength LED pointed at the photosensor was pulsed at 10kHz with a pulse 1.4 V in amplitude and 50 ns in duration. The mean of the charge distribution will be used as a measure of the photon flux.

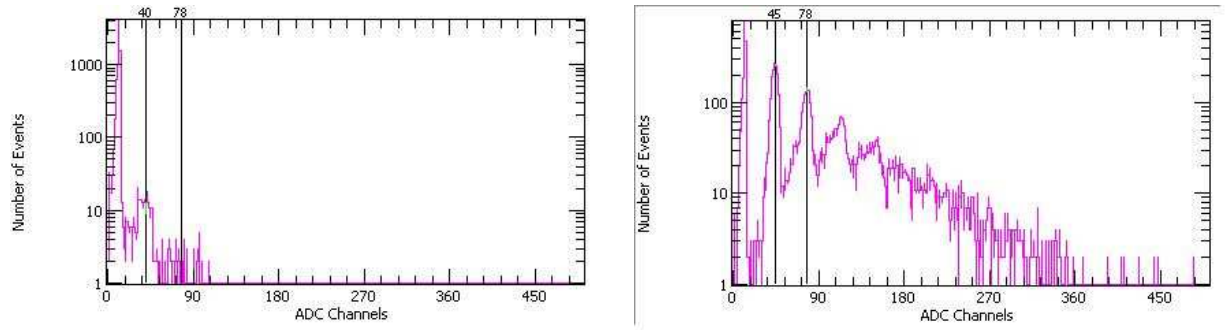

Figure 3.5: Hamamatsu sensor H68 ADC spectrum with preamplification, triggering on dark events (a) and triggering on the LED (b).

3.4 Dark Rate and Gain Functional Dependencies

We have mentioned that an ideal sensor will have a low dark rate and a high gain. The higher the gain, the lower the uncertainty on the total light yield measured by the ADC and the lower the dark rate, the fewer false coincidences there will be in detecting muons at light levels below a few p.e. It has also been pointed out that the dark rate of the photosensors depends on threshold, and both the gain and the dark rate of the sensors depend on bias voltage and temperature. In this section we present the results from a series of measurements we performed on the Hamamatsu MPPCs in order to quantify these dependencies.

3.4.1 Dark Rate vs. Threshold

Dark rate is an important background to measure because high dark rates may swamp the real signal, especially at low light levels which we expect to encounter in SMRD. Knowing the dark rate also will allow a calculation of false coincidences in the cosmic ray muon measurements. So it is important to accurately determine the dark rate for each sensor over the range of thresholds that can be expected. For each of the sensors H65, H67, H69 we have measured the dark rate using a NIM scaler at thresholds starting at 10 mV, which for our setup corresponds to less than half of one p.e., up to 120 mV (or about 5 p.e.) in 2 mV increments (Figure 3.6). The rates were measured for one second at each point. We observe a sharp drop in dark rate as the threshold of one p.e. is surpassed as expected. There are also drops in rate at 2 p.e. and 3 p.e. but the drops become less well defined for higher p.e. due to the broadening of the charge spectrum peaks. It should also be noted that the regions between the drops are not as flat as expected. This may be explained by a second avalanche occurring in the same pixel before the charge from a previous avalanche has been evacuated.

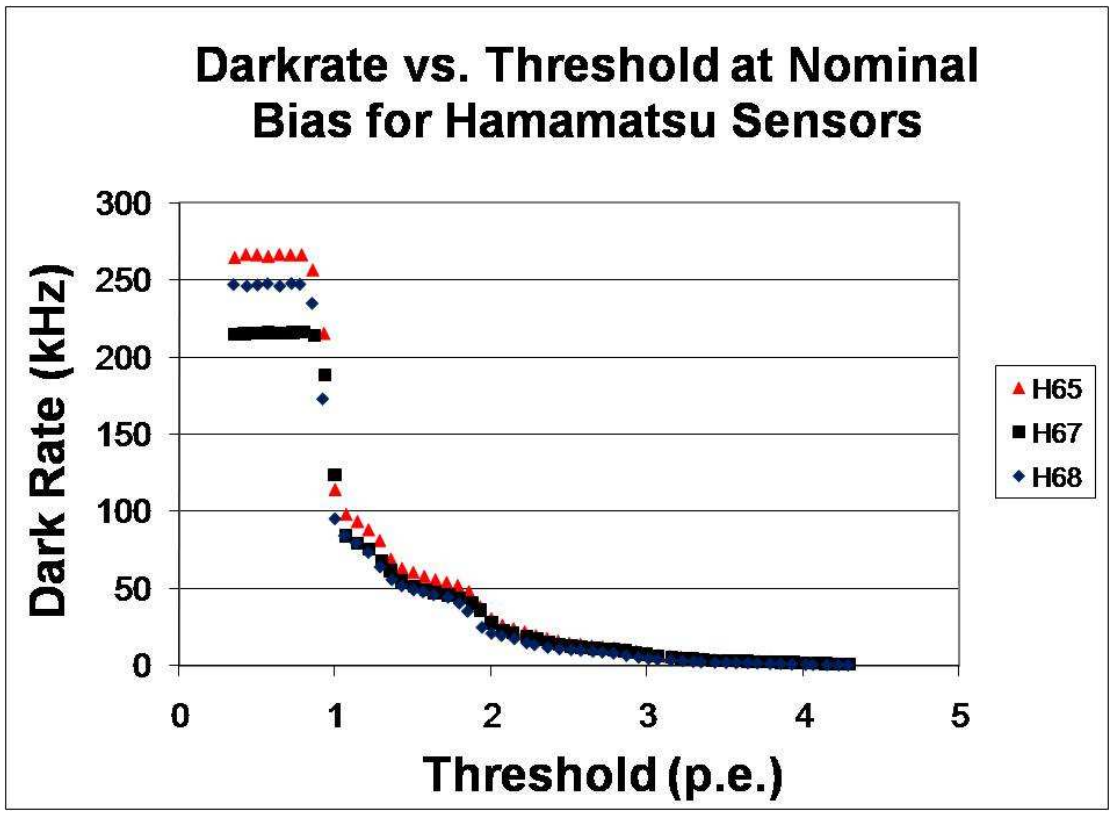

Figure 3.6: Dark rate as a function of threshold for three photosensors.

Table 3.1: Nominal bias voltages for the test sensors.

Sensor	Nominal Bias Voltage (V)
h60	70.30
h61	70.55
h62	70.01
h63	70.07
h64	70.11
h65	70.15
h66	69.99
h67	70.57
h68	70.21
h69	70.19

3.4.2 Dark Rate and Gain vs. Bias Voltage

The Hamamatsu test photosensors have a nominal supply voltage tuned so that the gain of all sensors is 7.5×10^5 (at 25°C). The same gain might require different bias voltages and therefore the dark rate may be different between sensors. Constant gain allows more straightforward comparison of light yield between modules, while constant dark rate makes it easier to determine the rate of muon detection and false coincidence rate. For the SMRD we will adjust the bias voltage for a constant dark rate, because the rate is the more important parameter for SMRD. The gain must then be measured at each bias voltage so light yield comparisons can be made as well.

We have measured the dark rate and gain as a function of the bias voltage for three Hamamatsu sensors. The nominal supply voltage for the MPPCs is about 70V. The manufacturer specified nominal bias voltages for each sensor are listed in Table 3.1. We tested the dependence of the gain and the dark rate on the bias voltage within a range of $\pm$ 1-2 V of the nominal bias voltage and have plotted our results in Figures 3.7 and 3.8 respectively. Over the range 68-70 V both the gain and the darkrate are linear. Applying a linear fit, we find that the dark rate increases at a rate of 1.3-1.8$\times 10^5$ Hz/V and the gain increases at 1.2×10^6 per V increase in bias voltage.

3.4.3 Dark Rate and Gain vs. Temperature

Temperature may be unstable in the magnet yokes at SMRD. Any fluctuations will likely be long duration due to the high thermal inertia of the yokes. Temperature sensors will be installed in the endcaps of some scintillators to monitor the temperature for changes. But in order for these data to be useful for temperature corrections, dark rate and gain must first be measured as a function of temperature for each of the sensors. We have performed these tests for three of the prototype Hamamatsu photosensors by heating them in an oven

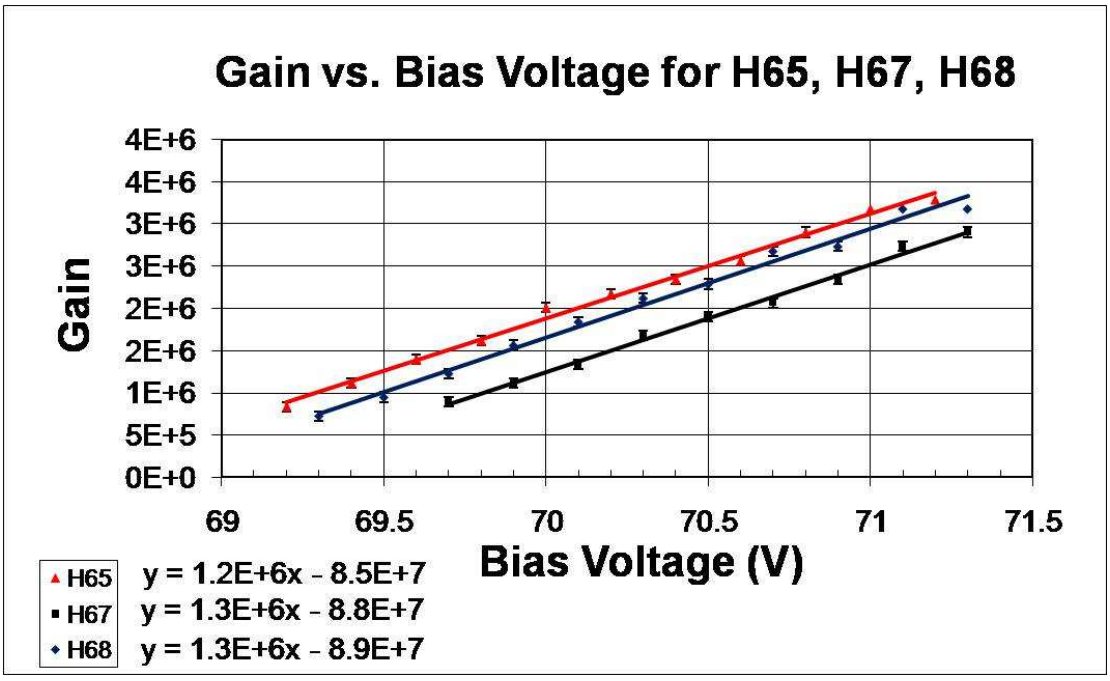

Figure 3.7: Gain vs. bias voltage for three Hamamatsu photosensors. Uncertainties shown are equal to one ADC channel uncertainty in peak position.

and then letting the oven cool over a period of a few hours while measuring the gain and dark rate once about every degree of temperature change. Figure 3.9 shows the darkrate of three photosensors vs. operating temperature. Figure 3.10 shows the gain of two of these same sensors as a function of temperature.

The temperature response of the sensors is linear over the range measured in both the gain and darkrate. Performing a linear fit we find the temperature coefficient for dark rate to be between 10.7 and 11.8 kHz/°C. For gain it is -1.15 and -1.25 ADC channels per °C which equates to -6.0 $\times 10^4$ and -6.5$\times 10^4$ respectively in electrons per incident photon per °C. The dark rate will be fixed for all sensors by the bias voltage, and the average temperature coefficient for the three sensors we measured is 11.1 kHz per °C which corresponds to only a 4% increase in dark rate at 25°C. Furthermore, there are not expected to be variations in temperature in the yokes greater than a few degrees C because they will be in a climate controlled environment. Based on these three facts we conclude that it will not be necessary to measure the dark rate temperature dependency for all 4000 sensors but only for a small, representative sample of sensors (perhaps a few more in addition to those we have presented here). Then it would be appropriate to use the mean value of these measurements for the temperature coefficient to make the temperature correction for all sensors. The gain however will be different for each sensor due to the different bias voltages, so the temperature dependence of gain should be measured for all of them.

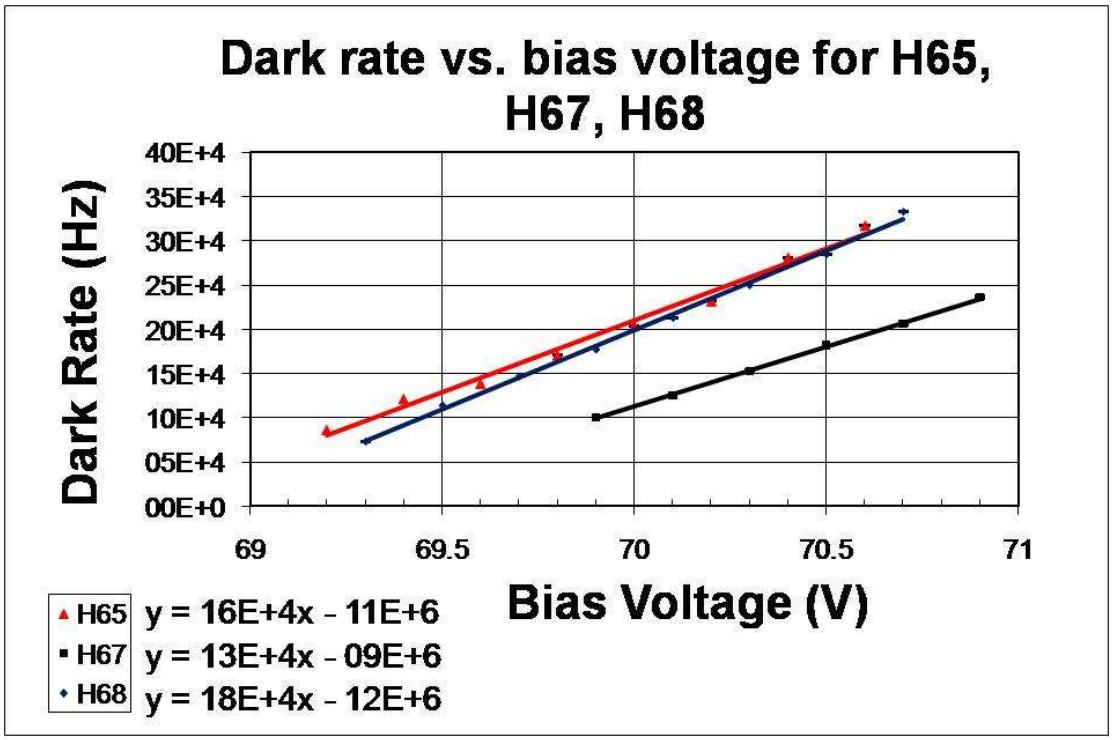

Figure 3.8: Dark rate vs. bias voltage for three Hamamatsu sensors. Uncertainties are statistical.

3.4.4 Dark Rate and Gain vs. Time After Power-On

Shortly after we began to use the MPPCs, we noticed a difference in the dark rate depending on how soon we began a measurement following the initial power-on of the device. Follow up tests showed that both the dark rate and the gain show initial spikes for the first 10 minutes or so following power-on (see Figures 3.11 and 3.12). The spikes are present regardless of whether the sensor is power cycled in quick succession or is powered on after a long period of inactivity. The cause is not fully understood, but it is suspected that temperature fluctuations due to power dissipation in the sensor and/or preamplifier may be the reason. The temperature change that would correspond to a 4 kHz increase in dark rate as observed over a ten minute time period would be only 0.25 °C and the observed gain increase of 0.5 ADC channels corresponds to a temperature change of 0.4 °C. It is reasonable to expect that temperature fluctuations of this magnitude could occur in the sensor over the duration of these measurements. We conclude from this test that, although these effects are small, it is still important to allow sufficient time for the temperature to stabilize prior to commencing with other measurements.

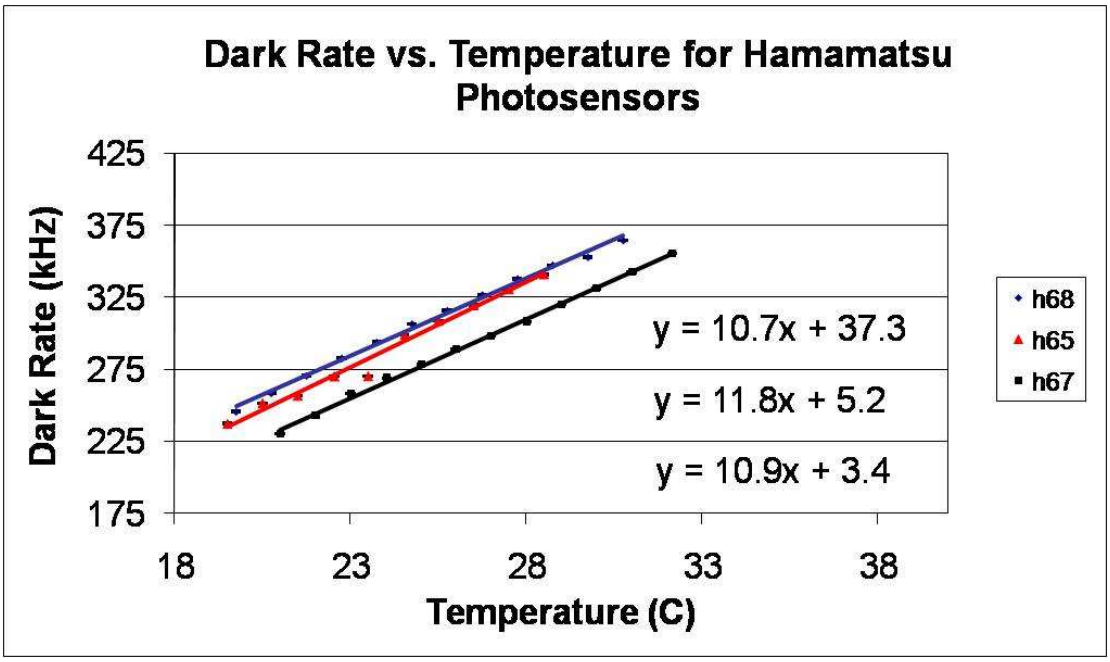

Figure 3.9: Dark rate vs. temperature for three photosensors. Uncertainties are statistical.

3.5 Aging Studies: Long-Term Dark Rate and Gain

T2K is planned to run for 10 years of data taking to achieve sufficient statistics for measuring θ_{13}, and so the long term stability of the photosensors is a critical parameter to measure. The Si-based photosensors have not been used in any other experiment and were developed so recently there are no long term data available. After only a few months of testing our samples of the MRS APDs, only three sensors survived out of the original eight. This was a great cause for concern, we naturally wanted to determine whether the Hamamatsu MPPCs would be more reliable long term.

Between the time the first batch of MPPCs was produced, and the time the SMRD assembly began were only a few months so we used an oven to heat the photosensors to 80 °C to speed the aging process. Thus we were able to simulate the deterioration over lifetime of the experiment in only a few months.

We used three photosensors H65, H67, and H68 for the experiment. They were taken out of the oven and the gain and dark rate were measured at room temperature at nominal bias voltage on a daily basis. The nominal bias voltages are listed in Table 3.1. We measured the dark rate above 0.5 p.e. Because the length of time after the sensor has been powered up affects the gain and dark rate, our procedure required a wait time of exactly 5 minutes between power up and measurement of the dark rate and gain (ideally we might wait longer but as long as we are consistent the power-up effect can be taken into account). We also measured the ambient air temperature near each photosensor immediately prior to measuring the dark rate and gain each day to calibrate out any temperature fluctuations

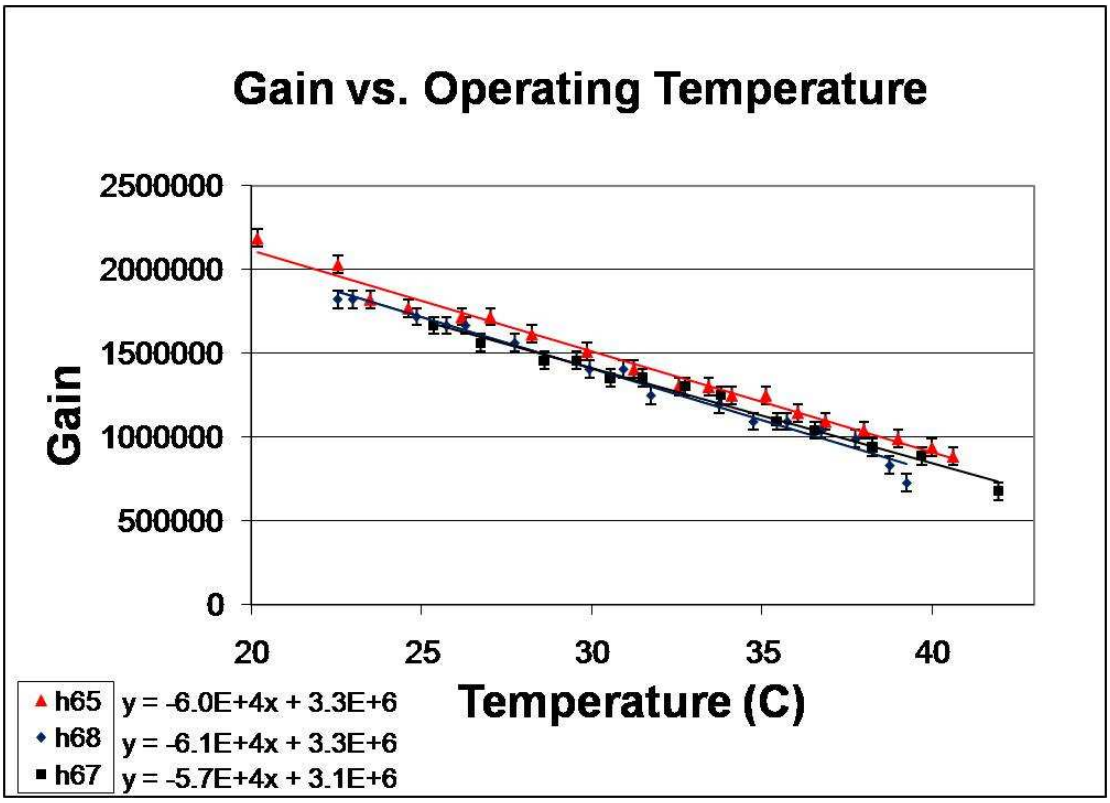

Figure 3.10: Gain vs. temperature for three Hamamatsu sensors. Uncertainties shown are for a one ADC channel uncertainty in peak position.

in the lab. The average temperature from six temperature sensors was taken for each data point. Figure 3.13 shows these fluctuations in the lab temperature over the course of the measurements. We measured the dark rate by taking measurements for ten time intervals of one second duration for each sensor using the NIM scaler and averaging them. The gain was measured using an LED aimed at the photosensor, firing at 10 kHz with a width of 50 ns and amplitude of 1.4 V. 10,000 counts were recorded by the ADC in KMax and the first three photoelectron peaks were fit in Physics Analysis Workstation (PAW) [20] with Gaussian distributions. The separation between the mean of the first and second fit distributions was used to calculate the gain. Our results for the dark rate and gain are shown in Figures 3.14 and 3.15.

The temperature and bias voltage were recorded for each point and the gain and rate were corrected based on the temperature dependence and bias voltage measurements presented earlier to 20 °C and to the nominal bias voltage for each sensor. The uncertainties shown reflect the uncertainties in temperature, voltage, and statistical uncertainties. We see that there are short term fluctuations but the long term trend is flat for H65 and H68. H67 saw a jump in dark rate of about 10% in early December but was flat before and after. It shows no such jump in gain, and the jump corresponds to a jump in lab temperature at about the same time and so it is likely due to the temperature calibration. A fourth sensor,

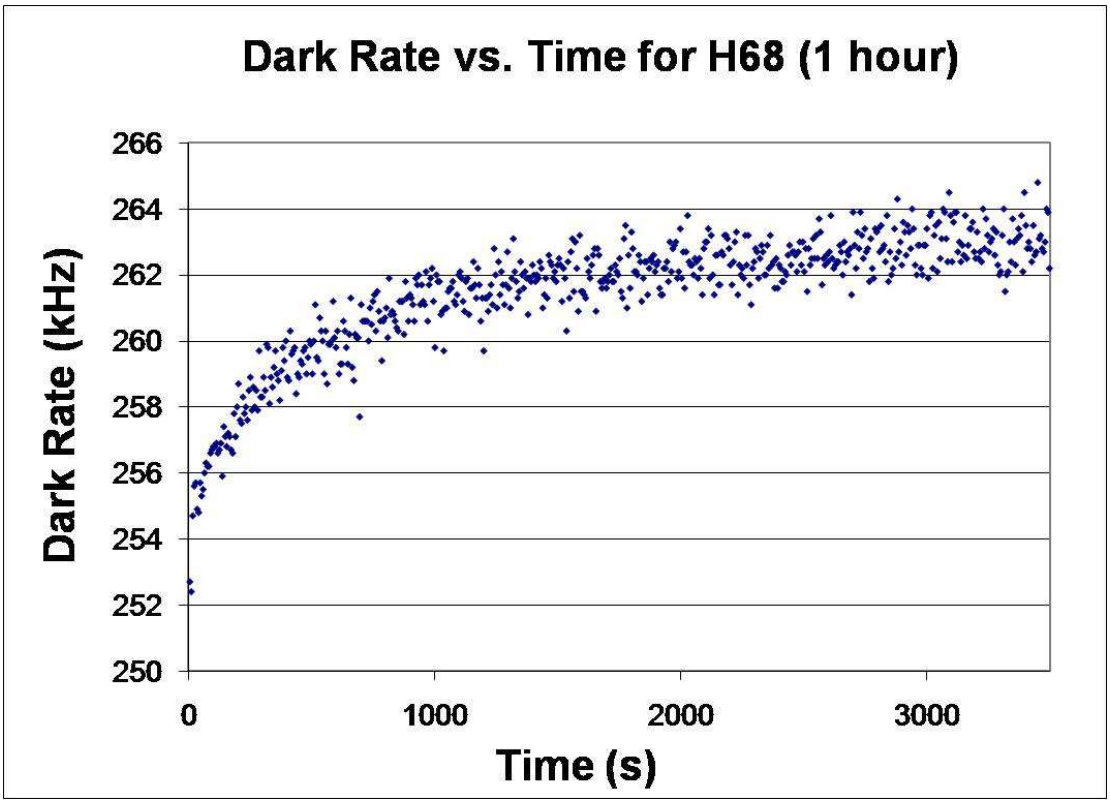

Figure 3.11: Dark rate vs. time after power-on. Counts recorded in one second spans taken at six second intervals.

H64, that was not heated is shown for comparison with the other three and also follows a similar trend over the period of measurement. From this test, we conclude that the sensors are stable over the period of more than 200 days under severe conditions.

In conclusion, we summarize the main results of this chapter. We have tested the Hamamatsu MPPC photosensors and measured the dependence of the dark rate and gain on temperature and bias voltage. We find that the gain increases at a rate of 1.3×10^6 for every one volt increase above the nominal bias voltage and that the dark rate increases at 1.3-1.8 $\times10^5$ Hz per one volt increase. A few more sensors should be tested to determine if these fluctuations are statistical. These should not need to be measured for all sensors. We also find that the average increase in dark rate for three test sensors is only 4% per °C at 25 °C. The gain decreases at about 4% per °C at 25 °C. Since the gain will vary from sensor to sensor, the dependence of gain on temperature should be measured for more test sensors. We also conclude from our aging studies that the photosensors are stable in dark rate and gain over time periods of several months.

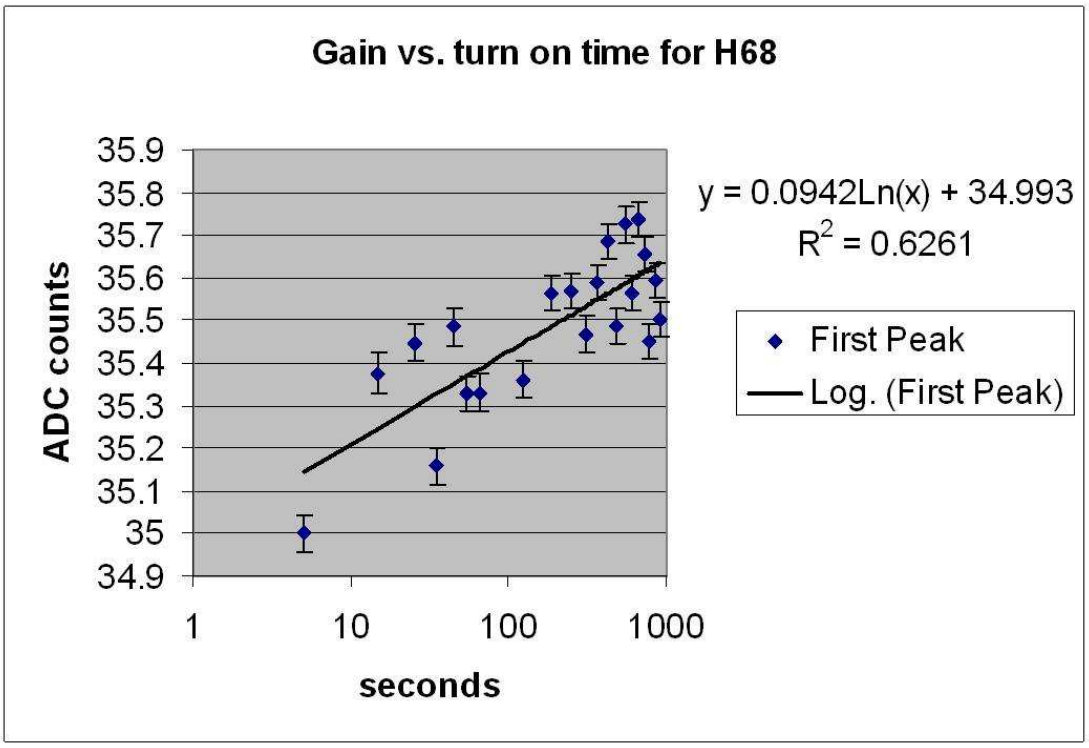

Figure 3.12: Gain vs. time after power-on.

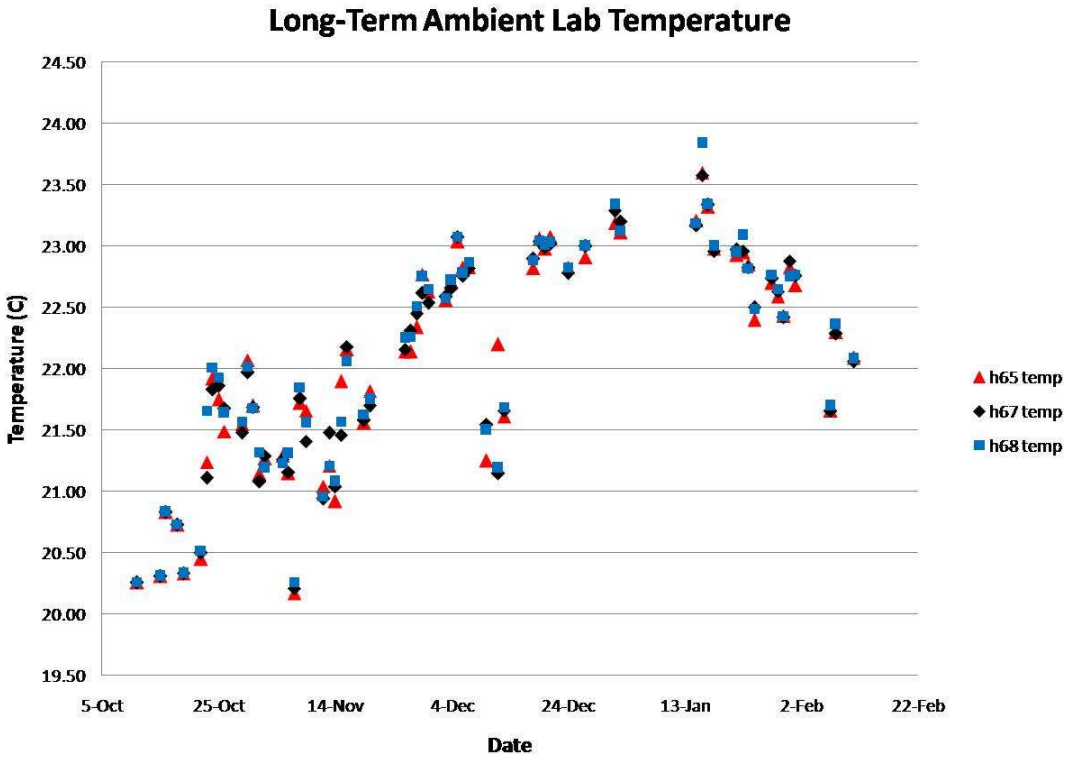

Figure 3.13: Long-term ambient temperature variations in the lab. Three temperature measurements were made each day, one each at the same time each of the three test sensors was measured. Each point represents the average value of six analog temperature sensors inside the dark box. The lab is 1-2 °C warmer in the winter months when the central heat was running.

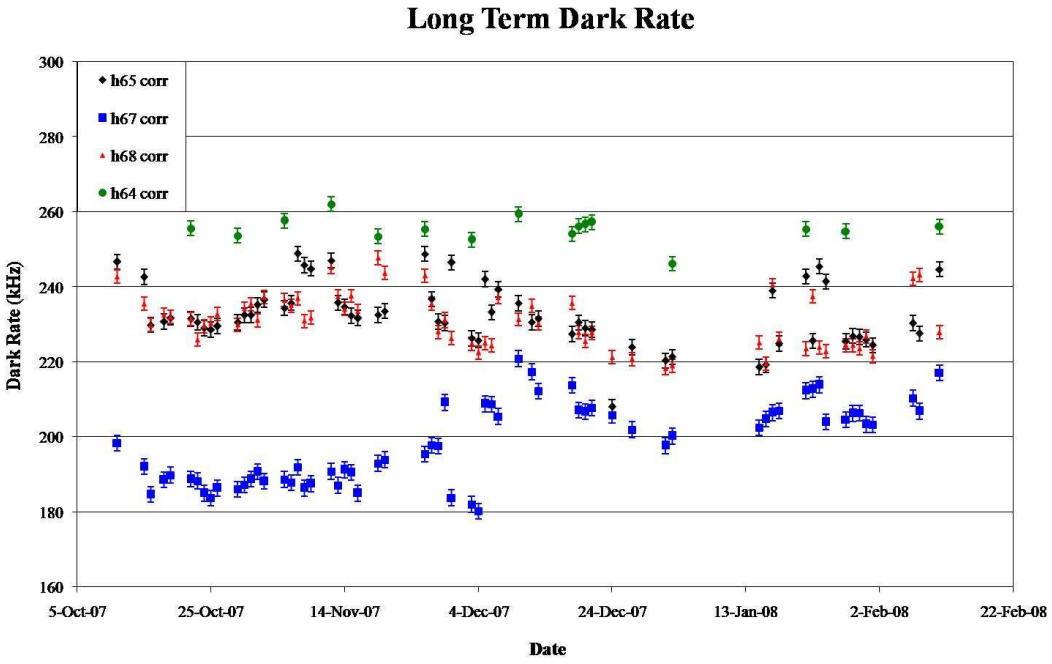

Figure 3.14: Long-term dark rate for four Hamamatsu photosensors. H65, H67, and H68 were kept at 80 °C while H64 was maintained at room temperature as the reference sensor.

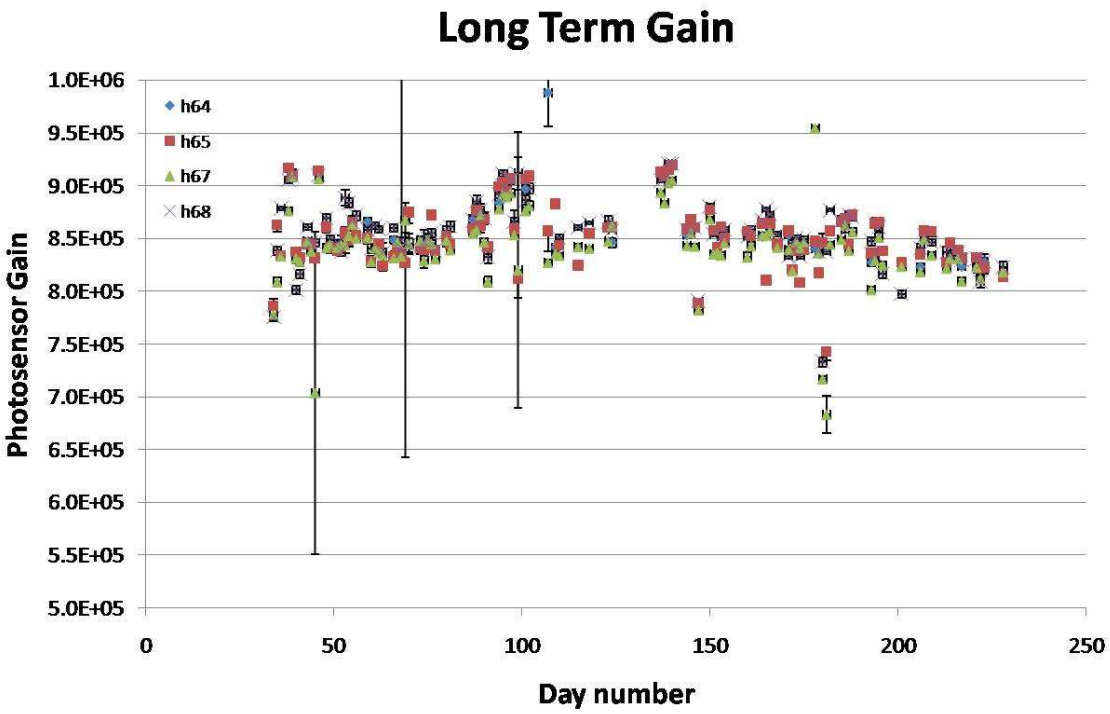

Figure 3.15: Long-term gain for three sensors aged in oven at 80 °C. Temperature correction has been applied. A fit is made to the photoelectron peaks and the gain is calculated as the difference between the first and second peaks. Uncertainties reflect uncertainty in Gaussian fit and uncertainty in temperature measurement.

Chapter 4

SMRD Scintillator Modules

4.1 Physical and Mechanical Properties

The scintillators for SMRD are organic plastic scintillators manufactured by the company Uniplast via an extrusion process. About 2000 will be needed to instrument the slots in the yokes. The outer surface of the scintillators is chemically coated with a thin, diffusely reflecting white film to trap light inside the scintillator.

Two different sizes of scintillator slabs will be produced to ensure a proper fit in the slots in the yokes. 768 slabs in total that are 87.0 cm long by 17.5 cm wide slabs will fill the gaps in the upper and lower limbs of the magnet yokes, while 1120 slabs in total that are 87.0 cm by 16.7 cm will fill the gaps on the two sides of the yokes. All scintillators will be 0.7 cm in height. Since the attenuation length in the scintillator is only about 10 cm [13], wavelength-shifting fiber with a longer attenuation length of about 3.6 m [12]) will be used to pipe the light out to the photosensors. The fibers will be inserted into a 2.5 mm deep groove machined into the surface of the scintillator. A photograph of one of the scintillator slabs is shown in Figure 4.1.

Originally, a number of straight fibers were planned to be inserted into the scintillator so there would be a uniform detector response and lateral position of a muon interaction within the slab could be determined (see Figure 4.2). The fiber in which the highest photon flux was observed would be the one closest to where the muon passed through. The lateral resolution would be better the more fibers were used (the figure shows seven). Each fiber requires a photosensor however, and the advantage of having lateral position information was minimal so it was determined that the limited project budget would be better spent instrumenting more gaps in the yokes. The minimum of a single fiber per slab would be used. A single fiber, even if placed at the center of the slab would be farther away from some parts of the scintillator than the attenuation length within the material. So instead the groove will be manufactured in an S-shaped pattern so that no part of the scintillator is farther away from the fiber than its attenuation length.

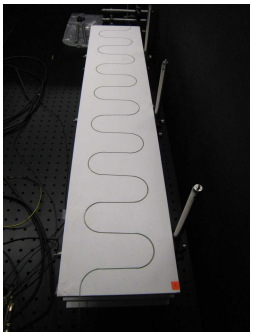

Figure 4.1: Photograph of one scintillator slab showing the fiber in the S-shaped groove and the white exterior coating.

Instrumenting both ends of the fiber with photosensors we can compare the arrival time of each signal, and knowing the speed of light within the fiber, we can then determine the longitudinal position of the muon interaction.

Figure 4.2: Early seven-fiber scintillator.

The fiber will be glued into the groove with BC-600 optical cement to provide optimum transmission of photons across the scintillator/fiber interface. The light transmission of BC-600 is greater than 98% [11]. It may also be covered with a diffusely reflecting material such as Tyvek to prevent photons from escaping around the fiber. The fiber will exit the scintillator on either end through a molded plastic endcap. The endcap will have a snap-on connector for mating the end of the fiber and the photosensor. The endcap will include space for a temperature sensor as well as mount points for a tool used to insert and remove the slabs and another tool to insert and remove the photosensors. See the picture in Figure 4.3. Each slab will be wrapped individually in stainless steel to form a light tight unit. Then four or five slabs will be bonded together to form a "module" to be inserted into the iron yokes. This modularity provides greater flexibility in case of damage during shipment. We have assembled a number of single slab test modules as shown in Figure 4.4.

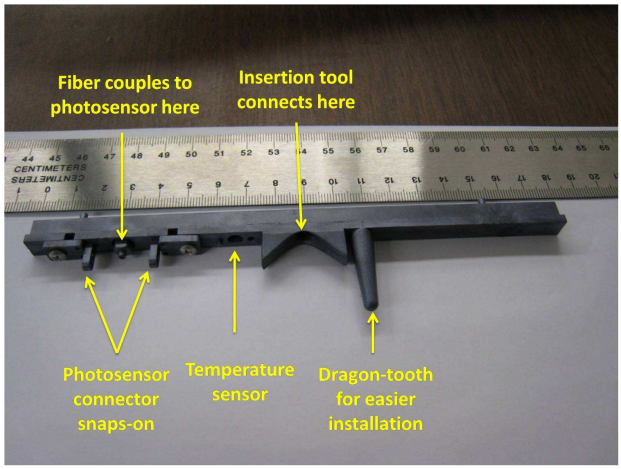

Figure 4.3: One of the endcaps ready for assembly.

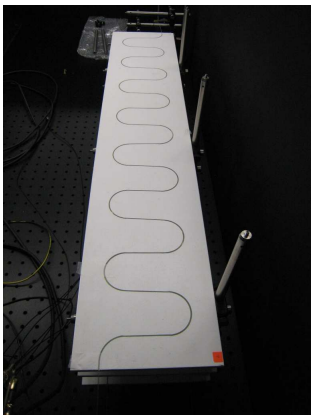

(a) Top view of scintillator with fiber inserted into groove prior to module assembly.

(b) Top view of scintillator with fiber covered by Tyvek prior to module assembly. At this point the fiber has been glued into the groove. The reflective side of the Tyvek is down, in contact with the fiber.

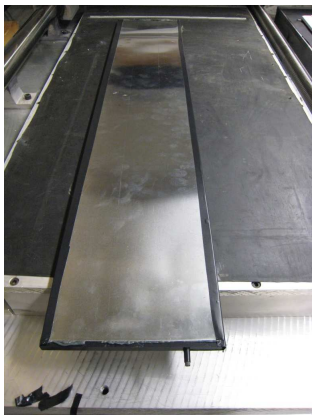

(c) Top view of scintillator after module assembly. The stainless steel skin and endcaps have been glued on using epoxy. The endcaps used here are not the final design.

(d) Top view of scintillator module on scanning table. This module is covered with black anti-static shielding instead of stainless steel.

Figure 4.4: Module Assembly

4.2 Wavelength Shifting Fiber

The wavelength-shifting fiber is 1 mm diameter double-clad Kuraray Y11. It contains a dopant which absorbs incident photons at about 450 nm wavelength and then re-emits

photons at about 500 nm. The absorption and re-emission spectra are shown in Figure 4.5. The reason the dopant is necessary is to match the peak emission wavelength to the peak photon detection efficiency of the photosensor. The fiber has an inner core surrounded by two layers of cladding of different index of refraction such that photons are internally reflected down the length of the fiber. There are two attenuation lengths in the fiber, a shorter and a longer one. The shorter of these is about 3.6 m while the length of fiber to be used in the modules is only 2.5 m, so there will be minimal loss of light.

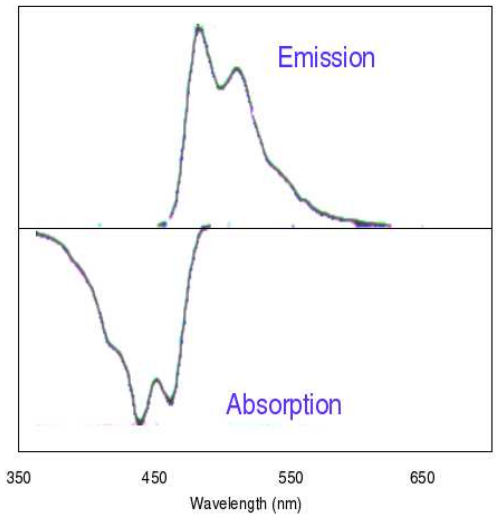

Figure 4.5: The Kuraray Y11 double-clad wavelength-shifting fiber absorption and re-emission spectra.

It is important that the fiber used have few if any defects because the levels of light are so low, if even a few photons are lost the results can be affected. So prior to cutting a length of fiber for insertion into the scintillator modules, it must be thoroughly inspected. We illuminate the fiber on one end with a blue LED and visually inspect for cracks or signs of damage (see Figure 4.6). A damaged fiber can manifest itself as a bright ring of light at some point along its length. A fiber such as this should be discarded and not be inserted into the groove. There are also non-uniformities within the dopant which can sometimes resemble a break but are usually more diffused. The difference between a damaged and undamaged section can be seen in Figure 4.7.

The fiber must couple to the photosensor at each end, so the ends of the fiber will be polished to ensure optimum photon transmission at this interface. There are two steps to the polishing. The fiber is first cut with a razor blade. Cutting a fiber frequently causes the outer cladding to separate from the core. So then the fiber end is sanded with 400 grit sandpaper to remove the material from the fiber end down to a point where the cladding is still attached to the core using a "figure-8" pattern which avoids a bias toward one side of the fiber that might cause the end to be angled. Next, the fiber is polished with 4-micron grit paper to remove any scratches left by the sandpaper. The results of the polishing

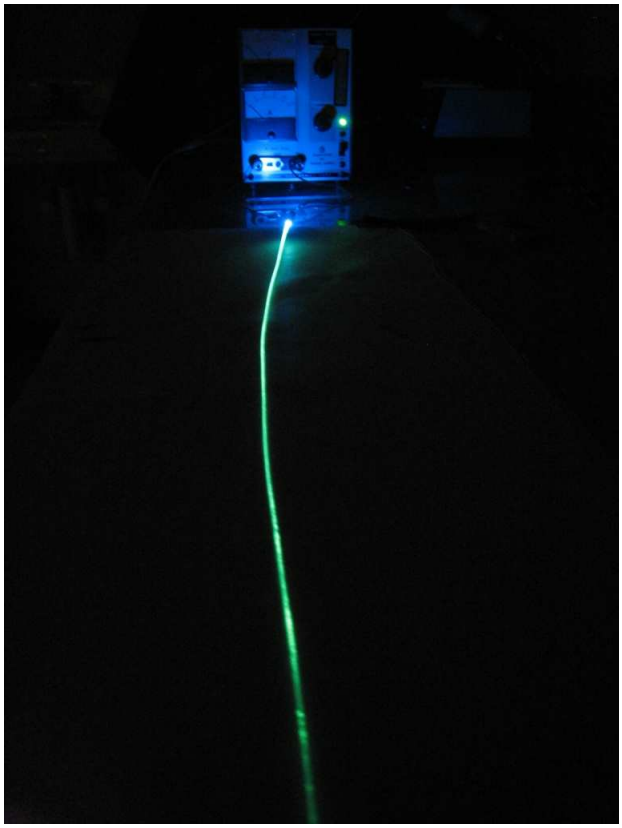

Figure 4.6: The fiber is visually inspected for defects prior to insertion into the scintillator module by shining an LED down one end and looking for breaks.

can be seen in Figure 4.8 (b) as compared to an unpolished fiber in Figure 4.8 (a). It is clear that prior to polishing the cladding has separated from the core of the fiber and after polishing there is no longer any separation. A few micro-scratches are still visible from the coarse sandpaper even after polishing with the fine grit paper but these do not measurably affect the light transmission. The effect of polishing on light yield (using an LED to illuminate the fiber) is seen in the charge spectrum in Figure 4.9. The mean of the distribution before polishing is 2.5 p.e. and after polishing is 4.0 p.e. This corresponds to a 60% improvement in light yield. The quality of the initial cut can vary, but with sufficient polishing, a fiber end of similar quality to that depicted in Figure 4.8 (b) can always be achieved.

One of the most critical aspects of the scintillator assembly is the connection between the fiber end and the photosensor. Since the fiber and the sensitive area on the test batch of photosensors are both 1.0 mm in diameter, it is vital that the fiber be centered on the photosensor's sensitive area to minimize light loss at the interface between the two. Figure 4.10 shows the effect of an off-center fiber-photosensor alignment. The sensor was moved in a grid pattern with respect to the stationary wavelength-shifting fiber end. The vertical and horizontal position increments were 0.5 mm. The fiber was illuminated by a blue LED and the ADC spectra at each point were recorded for 10,000 events each. The mean light

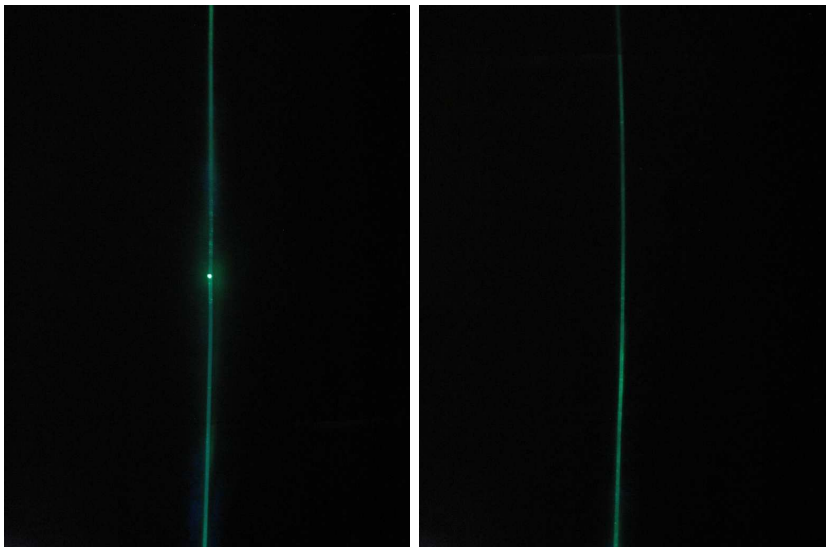

(a) A broken fiber is visible in the LED test.

(b) A good section of fiber with no major defects.

Figure 4.7: Fiber inspection.

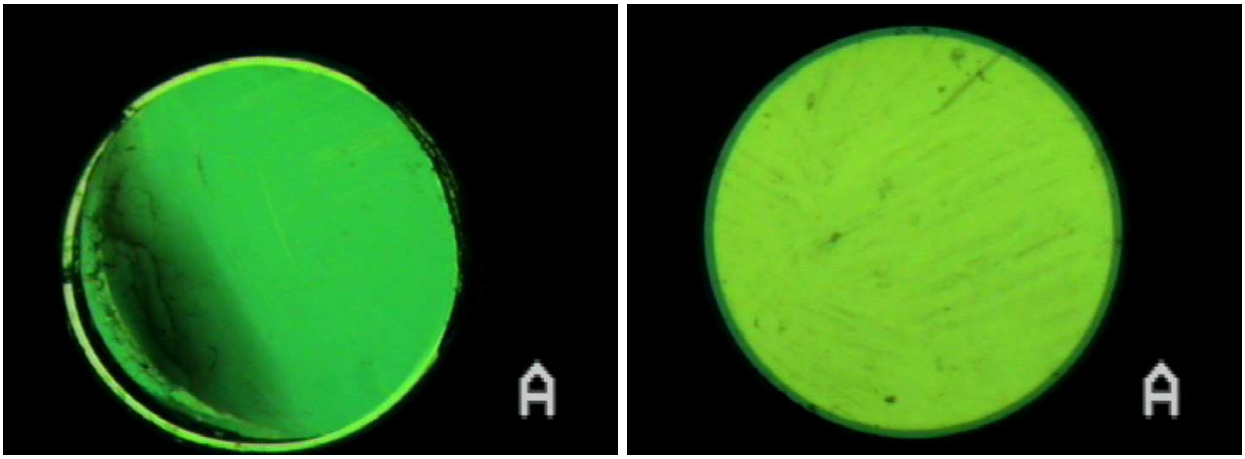

(a)

(b)

Figure 4.8: Microscope photograph of a 1.0mm diameter wavelength-shifting fiber end at 200X magnification prior to polishing (a) and after polishing (b).

intensity in photoelectrons is plotted on the color axis. We see that for a misalignment of only 0.5 mm the light yield falls off by a factor of two.

Since the SMRD photosensors will use a connector to make the connection with the fiber

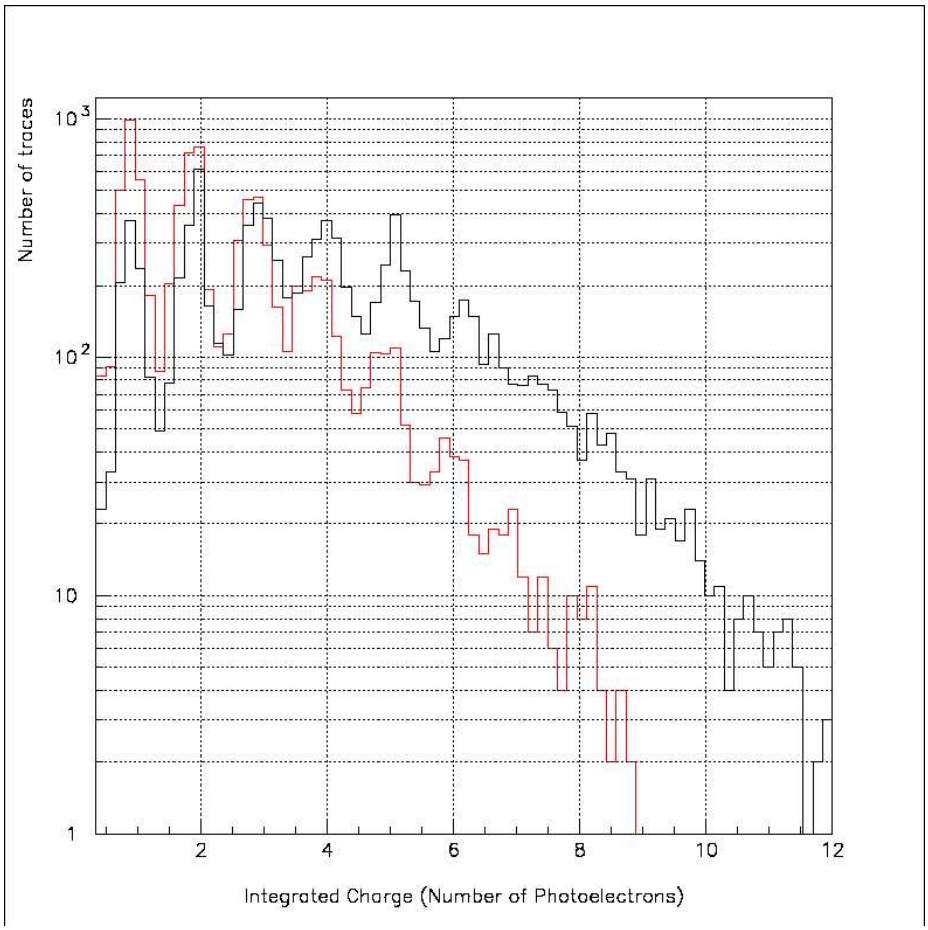

Figure 4.9: Charge spectra for polished fiber (black) compared with unpolished fiber (red).

end, the fiber alignment will not be as much of a concern. For our test sensors with sensitive area of 1.0mm it would be recommended that the tolerance on the connectors be 50 μm or better (the width of a single pixel on the photosensor) to minimize light lost at this interface. However, the production sensors will have a larger sensitive area of 1.3 mm; this larger size should allow for a less stringent requirement for the tolerance on the connectors. Other groups have also studied the effects on light yield of the fiber being at an angle with respect to the face of the sensor and the effect of not establishing contact with the sensor. While both of these are important in principle and can affect the light yield, they will not be a concern when using a connector to fix the sensor and fiber together. The SMRD connectors will make use of a foam spring to establish good contact between fiber and sensor.

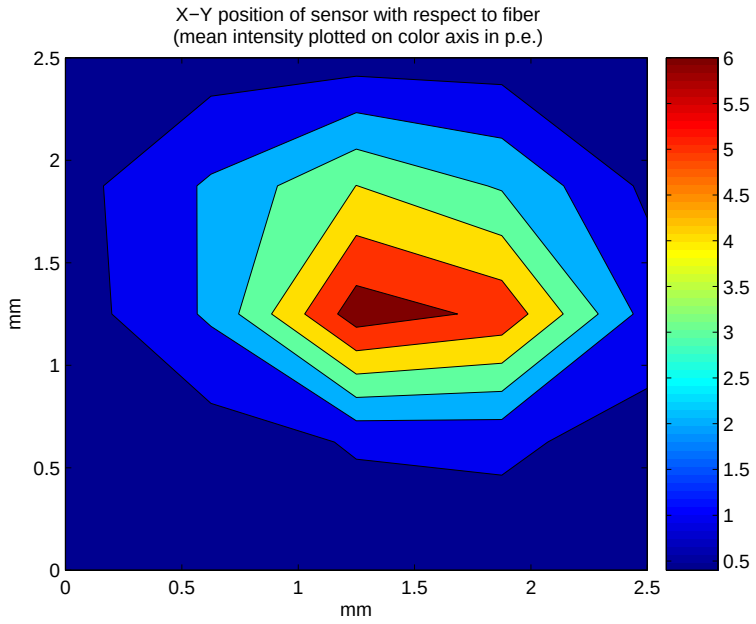

Figure 4.10: Fiber alignment test. Light yield is plotted on the color axis (in p.e.), and fiber-photosensor relative orthogonal position along x and y (in mm).

4.3 Atmospheric Muon Tests

Testing of the scintillators requires a source of muons, however manufactured muon sources are not available. Cosmic rays provide us with a natural source of muons. High energy protons and heavier nuclei interact in the upper atmosphere producing showers of charged pions and kaons which decay into muons and other particles. The total integrated flux of cosmic-ray atmospheric muons at sea-level is calculated by Tang, et. al. to be 1.9×10^{-2} $cm^{-2}s^{-1}$ [19]. The flux falls off roughly as $cos^2\theta$ of the zenith angle.

We have constructed a "muon telescope" for detecting atmospheric muons which we use as a trigger for testing the scintillators. The muon telescope consists of two "elements" nearly identical in size and appearance, each composed of a scintillator optically adjoined to a Photomultiplier Tube (PMT) and shielded from external photons with black electrical tape. Figure 4.11 shows one of these elements and its dimensions. The PMTs in each element are Hamamatsu R877 which have a nominal supply voltage of 1250 V and a gain of 5×10^5.

If the elements are placed one on top of the other, a coincidence between both elements is observed for a through-going muon. The PMT signals are sent through discriminators because the coincidence unit requires a digital input. The discriminators are set to a 20-25 mV threshold. A coincidence is counted if the signals arrive within 100 ns of each other. See Figure 4.12 for a schematic representation of the electronics of the muon telescope.

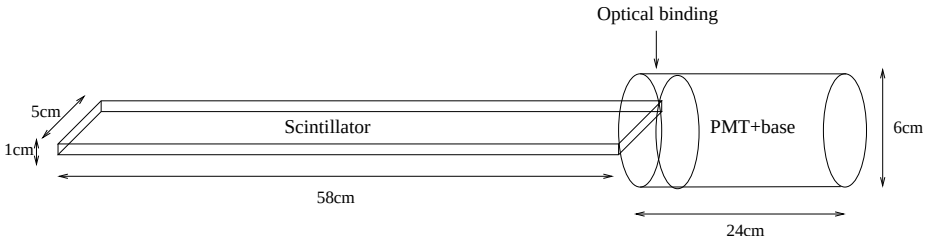

Figure 4.11: One element of the muon telescope and its dimensions.

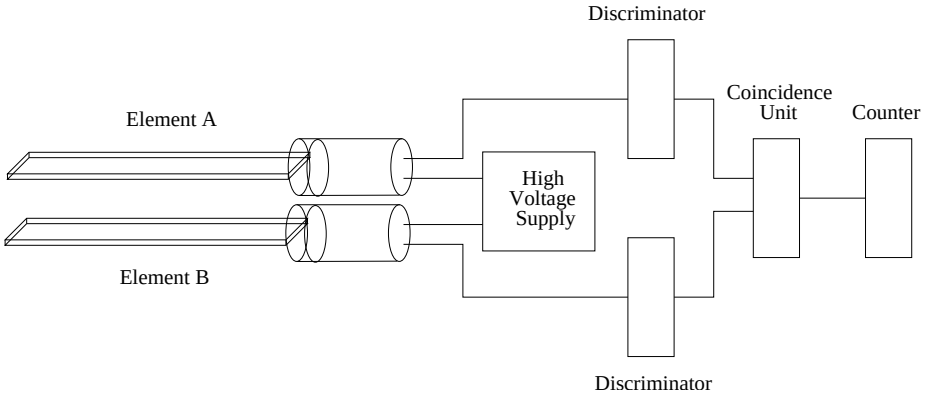

Figure 4.12: Schematic diagram of the muon telescope

The geometry of the setup and size of the elements will determine the observed rate. For highest rate but lowest position resolution, we place the elements parallel, one on top of the other. This gives about 300 cm^2 of overlap with an expected rate of about 6 Hz. For lower rate but maximal position resolution we place the elements at right angles, one on top of the other. This gives an overlap of only 25 cm^2 with a theoretical rate of 0.5 Hz. The vertical separation between the elements also affects the rate: larger separation will give lower rate due to exclusion of muons at angles away from the zenith. Table 4.1 shows that with zero separation we record a rate of 164 per minute or about 2.7 Hz with the elements parallel to each other. So we determine our efficiency to be a little less than 50%. This low efficiency could be due to the aging of the scintillators in the elements (which are a number of years old) or the connection between the scintillator and PMT.

We want to have a high position resolution on the test scintillator to precisely determine the location of any fiber damage so we will cross the muon telescope elements at right angles to each other, one above and one below the scintillator and assume that if a muon passes through both elements that it passed through the scintillator as well. The vertical spacing is 10 cm so the average rate is about 1 Hz. We will use the muon telescope coincidence signal then to trigger the ADC and collect data for the test scintillator.

Table 4.1: Muon telescope rate for several different vertical separation distances between elements. Average rate from 2 minute trials.

Vertical Spacing (cm)	Coincidence Rate (min^{-1})
0	164
8.5	70
10	59
33	24
60	8

4.3.1 Muon Interaction Light Yield Studies

To ensure muons incident on any part of the scintillator are detected, we want to test the positional dependence of light yield for muons passing through different parts of the scintillator. We obtain positional information by placing the overlap area of the muon telescope at three locations on the scintillator, in the center and 10 cm from either end. We expect that the sensor farther away from the muon interaction will observe the lowest light yield due to losses in the fiber. We are able to measure two scintillators at once with the scintillators stacked one above the other. Figure 4.13 shows a diagram of the setup and the three locations for the muon telescope. We use the muon telescope as a trigger and then record events in both of the test scintillators. The mean of the ADC spectra are taken as representative of the light yield of each slab. Table 4.2 shows the typical light yields (in p.e.) for photosensors at either end of the scintillator for the three positions of the muon telescope and the event-by-event sum is also shown. We confirm the expectation that the sensor farthest from the muon interaction observes the least amount of light. The sum is nearly the same for all three positions so we conclude that there is little or no positional dependence of muon detection efficiency. It is worth noting that the summed light yield in scintillator 6 is significantly lower than the yield for scintillator 8. This may not necessarily mean the scintillator is of a poorer quality but could instead be due to a poor photosensor/fiber connection, or an insufficiently polished fiber. As we saw previously, each of these effects can be large (in excess of 50%) so they may account for the difference. These types of measurements can be used as a test of scintillator quality, and below a certain threshold light yield the scintillator should be rejected for use in the SMRD. Low light yield means a loss in muon detection efficiency in the final detector. The light yield should be 10 p.e. or greater for each scintillator now to ensure that over the 10 year run time of the experiment, the age related degradation of the scintillators will not drastically reduce the efficiency.

For comparison, we show in Table 4.3 the same two scintillators prior to gluing the fibers into the groove. Taking the average of the three summed light yields, we see an increase in total light yield from 19.9 p.e. to 25.9 p.e. or 30% in scintillator 6, and 15.68 p.e. to 37.87 p.e. or 140% in scintillator 8 after gluing. The significance of these increases is in question because of the potential for large contributions from fiber polishing and alignment effects,

Table 4.2: Light output from scintillator 6 and 8 with fiber glued in groove, triggering on muon telescope at three positions.

Scintillator	Sensor	Position 1	Position 2	Position 3
6 (glued)	H66	19.37	15.34	12.57
	H69	10.16	12.67	15.96
	Sum	26.53	25.60	25.58
8 (glued)	H62	22.91	20.43	16.99
	H60	12.60	18.75	23.58
	Sum	34.90	38.72	40.00

however, both scintillators do show an increase in light yield after gluing the fiber.

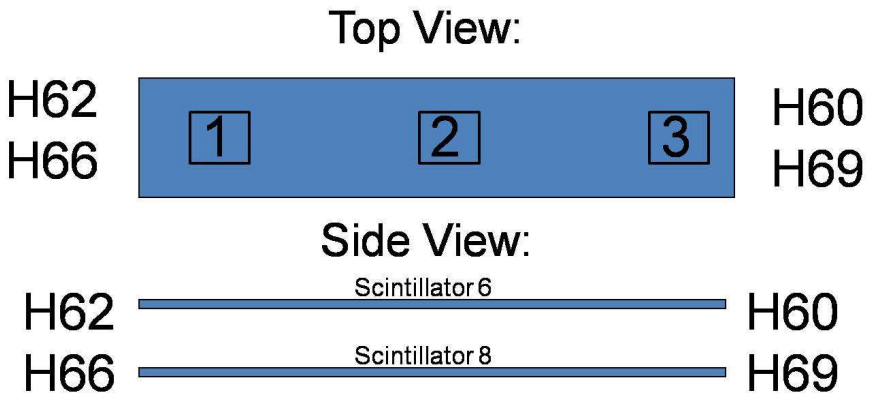

Figure 4.13: Schematic setup showing the three positions of the muon telescope and the locations of each photosensor (HXX) for atmospheric muon testing of two scintillators.

4.4 Radioactive Source Tests

It is important to be able to test the scintillator modules and verify they are in working order before they are installed into the yokes. Any fibers broken during installation or poor photosensor-fiber connections can drastically reduce the light output of a module. A number of contingency modules will be manufactured so that any modules deemed unsuitable for use will be replaced. Atmospheric muons could be used for these tests, however, as seen previously, the rate is very low (about 1 Hz) and ideally each scintillator will be tested at many positions. We determined that this rate is too low to make this method feasible in the time-line for construction. The alternative method is to use a radioactive source. The scintillators react similarly to high energy gamma-rays as to muons so the test results using a source should be indicative of what will be seen in the final experiment. And the rate for a source can be much higher than for atmospheric muons (depending on the source activity and corresponding gamma energy).

Table 4.3: Light output from scintillator 6 and 8 prior to gluing the fiber in the groove, triggering on muon telescope at three positions.

Scintillator	Sensor	Position 1	Position 2	Position 3
6	H66	10.98	13.03	16.14
	H69	14.43	11.79	9.83
	Sum	17.31	19.61	22.90
8	H60	8.71	15.17	18.64
	H62	14.01	11.19	9.28
	Sum	16.02	15.38	15.66

Table 4.4: Single photosensor rate vs. threshold for 25 μCi ^{137}Cs source (662 KeV gamma from Ba-137) and 10 μCi ^{60}Co source (1.17 MeV and 1.33 MeV gammas) and no source.

Threshold (p.e.)	^{137}Cs Count Rate (Hz)	^{60}Co Count Rate (Hz)	No Source Count Rate (Hz)
1.5	35500	37500	26167
2.5	2283	2750	1198
3.5	183.3	325	66.67
4.5	15	40.33	4.611

We have tested two gamma-sources: a 10 μCi ^{60}Co source and a 25 μCi ^{137}Cs source. ^{60}Co emits two gammas per decay: a 1.17 MeV and a 1.33 MeV gamma, and ^{137}Cs decays to ^{137}Ba which emits a single 662 KeV gamma. We measured the rate of events at one end of the scintillator with a single photosensor connected to the fiber to determine which source achieves a higher rate. It was found that the cobalt source gave a higher rate at every shown threshold (see Table 4.4). This is to be expected because of the two gammas per decay and higher energy per gamma. We therefore performed all subsequent tests with the ^{60}Co source.

Next, it was necessary to determine at what threshold the rate of source events rises above the dark rate. We measured the coincidence rate between the photosensors at the two ends of the scintillator rather than a single photosensor as in the previous data. The results are shown in Table 4.5. We conclude that a threshold of 2.5 p.e. ensures a high source to dark rate ratio and recommend use of this threshold for measurements with this source.

The goal of using the source is to detect broken fibers or other damage prior to installation of the scintillator modules into the yokes. So we also need to determine the degree of damage that is detectable. So we intentionally damaged the fiber at one location on the scintillator and measured the source rate at four positions near the break (see Figure 4.14). Our results are tabulated in Table 4.6. We used the threshold of 2.5 p.e. determined in the previous test. Here we have used a lead brick to collimate the source so that the gammas pass through a small, localized region of the scintillator. This results in rates that are somewhat lower than the previous uncollimated source data. We first measured the rates

Table 4.5: Coincidence rate vs. threshold 10 μCi ^{60}Co source compared with no source.

Threshold (p.e.)	^{60}Co (kHz)	No Source (kHz)	(%) Source Events
0.5	55	19.6	63
1.5	21	0.60	97
2.5	9	0.030	99.6
3.5	3.7	0.02	99.5
4.5	1.9	0.02	98.9

Table 4.6: Coincidence rate (Hz) for varying degrees of fiber damage with source at four positions. Uncertainties are statistical; 30-50Hz for data shown.

Degree of Damage	Position (a)	Position (b)	Position (c)	Position (d)
no cut	2156	2163	2222	2022
1 cut	2096	2300	2175	1897
2 cuts	1841	2199	2104	1809
3 cuts	1994	1920	1655	900

at each of the four positions with an undamaged fiber. Then we damaged the fiber by cutting through the outer cladding of the fiber with a razor blade at the position shown in the diagram and re-measured the rates. We made a second cut adjacent to the first cut, half-way through the fiber, and re-measured the rates. And finally we made a third cut, this time all the way through the fiber, adjacent to the previous two cuts. We find that there an approximately 10% reduction in rate on either side of the break for minor damage and a 50% reduction for major damage. The rate can easily vary by 10% due to the fiber-photosensor connection which so unfortunately with this type of test, it may be difficult to detect minor damage in the fiber. A number of trials at the same positions could be run to get a distribution of fiber to sensor coupling and by this method it may be possible to verify damage at the 10% level. However, even with a single measurement, major damage (e.g. a fiber cut all the way through) will be made obvious by a rate reduction factor of two.

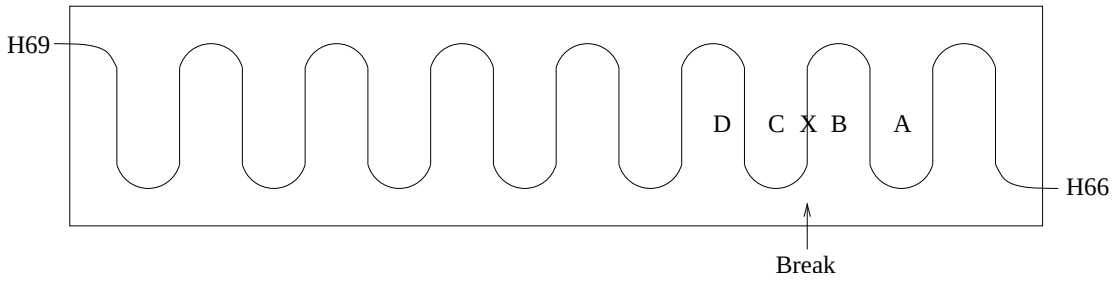

Figure 4.14: Setup for the fiber damage test showing the four source positions A,B,C,D and the location of intentional fiber damage between position B and C.

4.4.1 Scanning Pattern Optimization

In all of our tests thus far we have physically moved the source by hand. However this will be unfeasible in scanning thousands of scintillator modules so a computer-controlled, motorized scanning table will be used to speed up the process in final testing. The finished module will be set on the x-y scanning table (see Figure 4.15) and the source will be automatically moved to any number of programmable positions. The process is automated with the motion control and data acquisition both run from within KMax on the same computer. A simple pattern of 100 source positions down the center of the scintillator has been run and the mean light yield at each position is shown in Figure 4.16. We see that as the source is moved toward one photosensor the light yield rises in that sensor and falls in the opposite sensor. This is due to the absorption in the fiber. We should expect there to be a symmetry between the two curves, with them crossing at the midpoint of the scintillator. We see instead that they cross closer to the sensor represented by the blue curve, which most likely means that the fiber/sensor connection is better for the sensor represented by the red curve.

In conclusion, we summarize the main results of this chapter. Muon detection efficiency depends on high light yield. We have determined that a number of factors help increase the light yield of a scintillator. Polishing the fiber end is important and can lead to a 60% increase in light yield. Gluing the fiber into the groove may be even more important, providing an increase of 30-140% in light yield. The fiber photosensor connection was the largest effect for our test setup, reducing the light yield by a factor of two for 0.5 mm misalignment. However this should not be a concern for the final detector due to the custom connectors and larger sensitive area of the photosensor. We also have determined a testing procedure for the scintillators using a radioactive source. A 10 μCi ^{60}Co source gives greater than a 99% source events when compared with dark events at 2.5 p.e. threshold so this is the recommended threshold for subsequent tests. Using this threshold, we can detect a badly damaged fiber by observing a factor of two difference in rate on either side of the break. We have shown preliminary results from the automated scanning table and indicate that the table should be able to find light yield measurements for many positions on the scintillators in less than one hour per slab.

Figure 4.15: The scanning table.

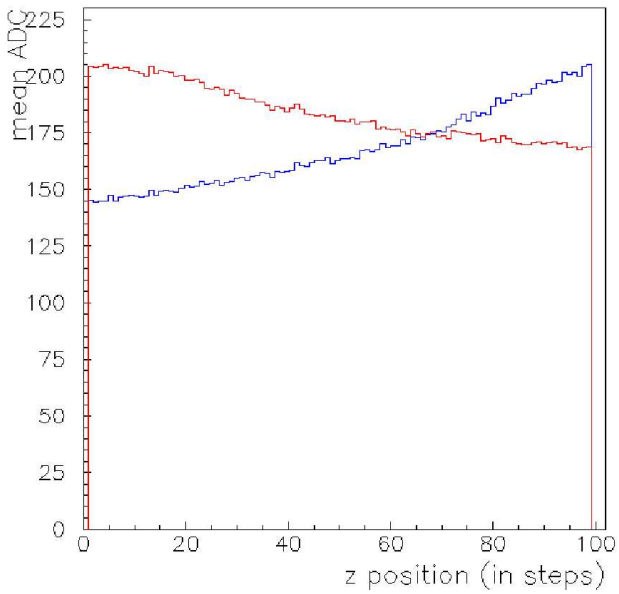

Figure 4.16: Data for 100 source positions along the center-line of the scintillator taken using the scanning table.

Chapter 5

Results and Conclusions

The principal goal of T2K is to measure the neutrino oscillation parameter θ_{13}. The muon-type neutrinos produced in pion decay at the JPARC facility will oscillate en route to the far detector at Kamioka. We will search for the appearance of electron-type neutrinos, and from Equation 1.1 a value of θ_{13} will be determined. The pions decay to muons and neutrinos, and their energies are related by Equation 2.1. The appearance probability depends on the energy of the neutrino which so by measuring the muon energy we can calculate the energy of the neutrino and determine the expected appearance probability. So two of the critical parameters to measure prior to and post-oscillation are the neutrino energy and the flavor composition of the beam. It is also important to measure π^0 background because they can be indistinguishable from ν_e events at the far detector.

ND280 sits in line with the far detector and observes the neutrino beam prior to oscillation. The observations must then be extrapolated to the far detector. The subdetectors at ND280 work together to measure the properties of the beam prior to oscillation. The TPC subdetector is responsible for measuring the energy of forward-going muons, but the task of measuring the energy of muons at large angles to the beam direction falls on the SMRD. The SMRD is a scintillation detector that will instrument slots in the iron yokes that surround the inner subdetectors. Muons will pass through alternating layers of iron and scintillator and their momentum can be determined by how many layers are penetrated. A high light yield in the scintillators will be required for a high muon detection efficiency. The light produced inside the scintillator must be piped out to the photosensor by a wavelength-shifting fiber due to the short attenuation length inside the scintillator. The fiber must make a good connection at both the interface with the scintillator and the interface with the photosensor to minimize light loss. The photosensors themselves must be impervious to magnetic fields, have a high photon detection efficiency, charge resolution, and gain, while maintaining a low dark rate, small physical size, and reasonable price.

We have tested the photosensors, scintillators, and wavelength-shifting fibers to be used in the SMRD subdetector of T2K. We have determined that the Hamamatsu MPPC sensors satisfy all of the criteria stated above, and are the best available device for use at SMRD.

These photosensors have been aged in an oven at high temperature and long-term dark rate and gain data have been collected to determine their long term stability. We observe no long term trends and we can conclude from these data that the sensors are stable over time to within about 10%.

The bias voltage will be adjusted independently for each photosensor in the SMRD to match the dark rates. So we have measured the dependence of the dark rate and gain on bias voltage. We find that both gain and dark rate increase linearly with bias voltage over the range of voltages studied. The dark rate vs bias coefficients vary at 1.3-1.8 $\times 10^5$ Hz per one volt increase in bias for the three sensors we tested so a few more sensors may need to be tested to determine whether these are statistical differences or not. The gain vs bias coefficients are about 1.3×10^6 per V increase in bias for the three test sensors. We conclude it will not be necessary to measure the bias voltage dependence of gain for each of the 4000 photosensors but once the gain is known at a single bias voltage it can be calculated using our coefficient when the bias voltage is adjusted.

Temperature fluctuations within the iron yokes are expected, so we have also measured the temperature dependence of the dark rate and gain of the photosensors to use in calibrating out these effects. Both are linear over the range of temperatures studied (about 20-30 °C; the gain decreases by 4% per °C at 25 °C while the dark rate increases by 4% per °C at 25 °C. We conclude that our average value of 11.1 kHz/°C can be used for the dark rate temperature correction coefficient for all sensors because the dark rate of every sensor will be set by the bias voltage to the same value and the temperature fluctuations are expected to be small. The dependence of gain on temperature should be measured for more test sensors.

We also tested the wavelength-shifting fiber and its interfaces with the other detector components. We found that polishing the fiber is important because it increases the light yield by as much as 60%. Gluing the fiber into the groove is also important, increasing the light yield by 30-140%. It should be noted however that these observed increases in light yield may be in part due to small differences in fiber/photosensor alignment. A misalignment of only 0.5 mm will reduce the light yield by a factor of two. However, this was mainly a problem in our test setup because the fiber diameter and the width of the sensitive area on the test sensors were the same. The production sensors will be larger than the fiber diameter and will use a custom connector to connect with the fiber so this issue will not be a concern.

We have also worked on developing an automated procedure for testing the scintillator slabs using a radioactive source. Within the time constraints for testing the 2000 scintillator slabs, atmospheric muons provide too low of a rate for testing. We have found that a 10 μCi ^{60}Co source provides a coincidence rate of 9 kHz at a threshold of 2.5 p.e. with 99.6% source events. This can be compared with a rate of about 1 Hz for the muon telescope. We have used this source to locate a damaged section of fiber, and conclude that the procedure will work well for badly damaged fibers. But, multiple measurements may be required to account for the effect of fiber sensor coupling if minor fiber damage is to be detectable.

Instead of moving the source by hand to different positions on the scintillator which takes a considerable amount of time and care, an automated scanning table is to be used to move the source. Preliminary results on the table indicate that it will work well, taking less than one hour to scan one hundred positions on each scintillator.

5.1 Recommendations for Further Research

The scanning table is nearly operational but further work must be done to resolve electronics issues and better optimize the scan pattern. The dark rate vs. bias and the gain vs. temperature should be measured for a few more sample sensors as soon as they become available. There are also a number of further studies to be done on the photosensors which will be of interest, not just to SMRD but also the other subdetector groups who use the same sensors. Cross-talk between adjacent pixels on the photosensor may be significant so this should be measured accurately. And in order to properly calibrate the detector, the absolute photon detection efficiency of the photosensors should also be measured. This is a difficult measurement to do because it requires a stable light source and an absolutely calibrated reference sensor. A relative photon detection efficiency measurement is somewhat simpler to make because one only needs a stable light source and does not need to know the incident flux. Each sensor may then be compared with all the other sensors and if an absolute efficiency measurement is made on one sensor then the absolute efficiency would be known of all the others.

Finally, we conclude that the results contained in this work will enable a better understanding of the SMRD subdetector which in turn is an integral part of the T2K experiment. T2K will be an important step forward in understanding the physics of neutrino oscillations and should provide the answers to long standing questions as well as potentially leading us to ask new ones.

Bibliography

[1] W.-M. Yao *et al.* (Particle Data Group), J. Phys. G 33, 1 (2006) and 2007 partial update for the 2008 edition

[2] The MiniBooNE Collaboration. arXiv:0706.0926v2

[3] The MiniBooNE Collaboration. arXiv:0704.1500v3

[4] The MiniBooNE Collaboration. doi:10.1103/PhysRevLett.98.231801

[5] The MINOS Collaboration. arXiv:hep-ex/0607088

[6] The LSND Collaboration. arXiv:hep-ex/0104049

[7] B. Aharmim *et al.* (The SNO Collaboration) doi:10.1103/PhysRevC.75.045502

[8] The Super-Kamiokande Collaboration. hep-ex/0501064

[9] M. C. Gonzalez-Garcia, Carlos Pena-Garay arXiv:hep-ph/0306001v2

[10] M. Apollonio *et al.* PLB 466 (1999) 415

[11] BC600 datasheet. www.detectors.saint-gobain.com

[12] Silva, J. *et al.* Nuclear Instruments and Methods in Physics Research A 580 (2007) 318-321.

[13] SMRD Techical Design Report. (Internal Document)

[14] Oser, Scott arXiv:hep-ex/0604021v1

[15] Perkins, Donald H. Introduction to High Energy Physics, Fourth Edition. Cambridge University Press. 2000.

[16] Altarelli, Guido and Klaus Winter (Eds.) Neutrino Mass. Springer. 2003.

[17] Zuber, Kai. Neutrino Physics. Institute of Physics Publishing. 2004.

[18] Mohapatra, Rabindra N. and Palash B. Pal. Massive Neutrinos in Physics and Astrophysics, Third Edition. World Scientific. 2004

[19] Tang, Alfred *et al.* arXiv:hep-ph/0604078v2

[20] Brun, R. *et al.* PAW - Physics Analysis Workstation, CERN Computer Centre Program Library Long Write-Up. 1988.

Vita

Kevin was born in Montrose, Colorado, in 1982, where he grew up and graduated from high school. He moved to Boulder, Colorado, in the fall of 2000 to attend the University of Colorado. He graduated in December 2004 with a Bachelor of Arts in physics. After a semester off from school, Kevin then moved to Baton Rouge, Louisiana, in May of 2005 and was a graduate student at Louisiana State University until the completion of this work in August 2008. While enrolled at Louisiana State University, he was additionally involved in the Sudbury Neutrino Observatory Collaboration and he taught introductory physics laboratories and recitations.